

# The order of macrophage 4D genome coordinates gene transcription during differentiation and infection

Gang Cao (✉ [gcao@mail.hzau.edu.cn](mailto:gcao@mail.hzau.edu.cn))

Huazhong Agricultural University <https://orcid.org/0000-0003-0761-7305>

**Da Lin**

State Key Laboratory of Agricultural Microbiology, Huazhong Agricultural University, Wuhan, China.

<https://orcid.org/0000-0003-0585-821X>

**Weize Xu**

Huazhong Agricultural University

**Ping Hong**

National Key Laboratory of Crop Genetic Improvement, Huazhong Agricultural University, Wuhan, China.

**Chengchao Wu**

State Key Laboratory of Agricultural Microbiology, Huazhong Agricultural University, Wuhan, China.

**Zhihui Zhang**

State Key Laboratory of Agricultural Microbiology, Huazhong Agricultural University, Wuhan, China.

**Siheng Zhang**

State Key Laboratory of Agricultural Microbiology, Huazhong Agricultural University, Wuhan, China.

**Lingyu Xing**

State Key Laboratory of Agricultural Microbiology, Huazhong Agricultural University, Wuhan, China.

**Bin Yang**

Huazhong Agricultural University

**Wei Zhou**

Huazhong Agricultural University

**Qin Xiao**

State Key Laboratory of Agricultural Microbiology, Huazhong Agricultural University, Wuhan, China.

**Jinyue Wang**

State Key Laboratory of Agricultural Microbiology, Huazhong Agricultural University, Wuhan, China.

**Cong Wang**

State Key Laboratory of Agricultural Microbiology, Huazhong Agricultural University, Wuhan, China.

**Yu He**

State Key Laboratory of Agricultural Microbiology, Huazhong Agricultural University, Wuhan, China.

**Jiangwei Man**

National Key Laboratory of Crop Genetic Improvement

**Xiaofeng Wu**

State Key Laboratory of Agricultural Microbiology, Huazhong Agricultural University, Wuhan, China.

**Xingjie Hao**

Huazhong University of Science and Technology

**Zhe Hu**

State Key Laboratory of Agricultural Microbiology, Huazhong Agricultural University, Wuhan, China.

**Chunli Chen**

Huazhong Agriculture University

**Zimeng Cao**

Yangtze University

**Rong Yin**

Wuhan University

**Zhen Fu**

University of Georgia <https://orcid.org/0000-0001-6293-9329>

**Guoliang Li**

Huazhong Agricultural University <https://orcid.org/0000-0003-1601-6640>

---

## Article

**Keywords:** single-cell Hi-C method, TAD “degree of disorder”, genome organization

**Posted Date:** October 29th, 2021

**DOI:** <https://doi.org/10.21203/rs.3.rs-881693/v1>

**License:**  This work is licensed under a Creative Commons Attribution 4.0 International License.

[Read Full License](#)

---

1   **The order of macrophage 4D genome coordinates gene transcription during differentiation**  
2   **and infection**

3

4   **Author names**

5   Da Lin<sup>1,2,3,4#</sup>, Weize Xu<sup>1,2,3#</sup>, Ping Hong<sup>5,6,7#</sup>, Chengchao Wu<sup>1,2,3</sup>, Zhihui Zhang<sup>1,2,3</sup>, Siheng Zhang<sup>1,2,3</sup>,  
6   Lingyu Xing<sup>1,2,3</sup>, Bing Yang<sup>1,2,3</sup>, Wei Zhou<sup>1,2,3</sup>, Qin Xiao<sup>1,2</sup>, Jinyue Wang<sup>1,2</sup>, Cong Wang<sup>1,2,3</sup>, Yu He<sup>1,2,3</sup>,  
7   Jiangwei Man<sup>4,5,6</sup>, Xiaofeng Wu<sup>1,2,3</sup>, Xingjie Hao<sup>8</sup>, Zhe Hu<sup>1</sup>, Chunli Chen<sup>9,10</sup>, Zimeng Cao<sup>11</sup>, Rong Yin<sup>12</sup>,  
8   Zhen F. Fu<sup>13</sup>, Guoliang Li<sup>2,4,5,6\*</sup> and Gang Cao<sup>1,2,3,4\*</sup>

9

10   **Affiliations**

11   <sup>1</sup>State Key Laboratory of Agricultural Microbiology, Huazhong Agricultural University, Wuhan, China.

12   <sup>2</sup>Hubei Hongshan Laboratory, Wuhan, China. <sup>3</sup>College of Veterinary Medicine, Huazhong Agricultural

13   University, Wuhan, China. <sup>4</sup>College of Bio-Medicine and Health, Huazhong Agricultural University,

14   Wuhan, China. <sup>5</sup>National Key Laboratory of Crop Genetic Improvement, Huazhong Agricultural University,

15   Wuhan, China. <sup>6</sup>Agricultural Bioinformatics Key Laboratory of Hubei Province, Hubei Engineering

16   Technology Research Center of Agricultural Big Data, 3D Genomics Research Center, Huazhong

17   Agricultural University, Wuhan, China. <sup>7</sup>College of Informatics, Huazhong Agricultural University, Wuhan,

18   China. <sup>8</sup>School of Public Health, Tongji Medical College, Huazhong University of Science and Technology,

19   Wuhan, China. <sup>9</sup>College of Life Science and Technology, Huazhong Agricultural University, Wuhan, China.

20   <sup>10</sup>Key Laboratory of Plant Resource Conservation and Germplasm Innovation in Mountainous Region,

21   Guizhou University, Guiyang, China. <sup>11</sup>College of Animal Sciences, Yangtze River University, Jingzhou,

22   China. <sup>12</sup>Medical Research Institute, Wuhan University, Wuhan, China. <sup>13</sup>Department of Pathology, College

23   of Veterinary Medicine, University of Georgia, Athens, GA, USA.

24

25   \*Correspondence to: guoliang.li@mail.hzau.edu.cn; gcao@mail.hzau.edu.cn

26   <sup>#</sup>These authors contributed equally: Da Lin, Weize Xu, and Ping Hong.

27 **ABSTRACT**

28 The highly organized three-dimensional genome is crucial for gene transcription. However, it  
29 remains elusive how the order of the genome architecture related to its function. Here, we  
30 developed a single-cell Hi-C method and proposed TAD “degree of disorder” as a measure of  
31 genome organizational patterns, which is correlated with the chromatin epigenetic states, gene  
32 expression and co-regulation, and chromatin structure variability in individual cells. Upon  
33 *Mycobacterium tuberculosis* infection, NF- $\kappa$ B enters into the nucleus, binds to the target genome  
34 regions and initiates systematic chromatin conformation reorganization. Furthermore, we  
35 identified a remote NF- $\kappa$ B enriched enhancer promotes the expression of PD-L1 through  
36 chromatin loop, which could be a potential anti-tuberculosis and even anti-tumor therapeutic target.  
37 The integrated Hi-C, eQTL, and GWAS analysis depicted the atlas of the long-range target genes  
38 of tuberculosis susceptible loci. Among which SNP rs1873613 is located in the anchor of a  
39 dynamic chromatin loop with LRRK2, whose inhibitor AdoCbl could be an anti-tuberculosis drug  
40 candidate. Our study provides comprehensive resources for the 4D genome of immunocytes and  
41 sheds insights into the genome organization order and the coordinated gene transcription.

42

43

44

45

46

47

48

49

50

51

52

53

54 **INTRODUCTION**

55 It has been many decades since Schrödinger posed the intriguing assumptions about the order  
56 or entropy in organisms and the chromosomes containing code-script of the individual's  
57 development and function in 1944<sup>1</sup>. While the hereditary code-script in the chromosomes has been  
58 well deciphered by sequencing now, there is still a big gap to understand the order or entropy of  
59 the chromosomes in the cell nucleus. It has been well-established that the folding and organization  
60 of the chromosomes in the nucleus is a process with a high degree of non-randomness and order<sup>2</sup>,  
61 <sup>3</sup>. Paradoxically, recent studies revealed that the three-dimensional (3D) genome architectures  
62 fluctuates dynamically among individual cells<sup>4</sup>. This dichotomy provokes the fundamental  
63 question how the order and stochasticity of the genome architecture coordinates with the precise  
64 transcription of genetic code-script.

65

66 In addition to genetic information, the chromosomes are also embedded with dynamic  
67 epigenetic codes functioning as blueprints for precise spatial and temporal gene transcription in  
68 different developmental stages in response to different stimuli<sup>5, 6</sup>. Epigenetic information can be  
69 encoded in the sophisticated organization of the 3D genome which can regulate the gene  
70 expression in space and time to fulfil distinct physiological tasks<sup>7, 8</sup>. Currently, little is known about  
71 how the genome organizational patterns fluctuate in different physiological states, especially at  
72 single cell level, such as immune cell during differentiation and immunological response.  
73 Monocytes are highly plastic immune cells which differentiate to different macrophages and play  
74 crucial roles in the first line of defense against pathogens<sup>9</sup>. During differentiation, monocytes  
75 transform their nucleus staining pattern<sup>10</sup>, implying a dynamic 3D chromatin structure. Upon  
76 infection, macrophages rapidly mature into different cell subtypes, such as M1 and M2  
77 macrophages, with distinct function and morphology<sup>11</sup>, of which the underlying epigenetic  
78 mechanisms are poorly characterized.

79

80 Tuberculosis (TB) is a global infectious health threat even more lethal than HIV/AIDS,

81 leading to approximately 1.3 million deaths and 10.4 million new cases worldwide annually<sup>12</sup>.  
82 Upon *Mycobacterium tuberculosis* (*M.tb*) invasion into the lung, pulmonary monocytes  
83 differentiate into pulmonary macrophages and are activated for immune defense against *M.tb*  
84 infection<sup>13</sup>. Extensive genome-wide association studies (GWASs) have identified many TB  
85 susceptibility loci, of which the majority are noncoding regulatory genetic elements<sup>14-17</sup>. However,  
86 which genes are the distal regulatory targets of these noncoding loci and how the SNPs influence  
87 the 3D genome remains unknown. The aim of this study is, therefore, to use this plastic THP-1  
88 monocytes and the differentiated macrophages as a model system to: 1) comprehensively  
89 investigate the 4D genome and dynamic epigenetic landscape of macrophages during  
90 differentiation and infection at single cell level; 2) investigate how the order and stochasticity of  
91 the genome architecture relates to the epigenetic modification and gene transcription.

92  
93

94 ***Development of single-cell indexed DLO Hi-C to decipher 3D genome of THP-1 cells during***  
95 ***differentiation and infection***

96 To investigate the 4D genome and epigenetic dynamics during differentiation into different  
97 lineages of macrophages, we used THP-1 cells, a highly plastic human monocytic cell line  
98 that can be differentiated into macrophage-like cells and activated by *M.tb*, as the cell model<sup>18, 19</sup>.  
99 In our study, we named the THP-1 cells before differentiation, after differentiation, and infection  
100 by *M.tb* as Thp1-mono, Thp1-macro, and Thp1-*M.tb* respectively. After PMA (phorbol 12-  
101 myristate-13-acetate) treatment, the nuclei of differentiated cells were transformed from ellipsoid  
102 to kidney-shaped (**Fig. 1a**), implying a possible 3D genome conformational change. The distinct  
103 morphology alternation of this cell line during different lineages also underlying a rapid  
104 reprogramming of gene expression profile during differentiation and infection (**Extended Data**  
105 **Fig. 1 a-c and Supplementary Table 1 and 2**). Consistent with this observation, the RNA-Seq  
106 data indicated that the expression levels of immune-related genes and M1 macrophage marker  
107 genes such as CD80, INHBA, CCR7 and TNF-a were significantly upregulated after infection  
108 (**Extended Data Fig. 1c**), indicating that the macrophages were transformed to the M1 phenotype.  
109

110 During these processes, we observed heterogeneous phenotypes between individual cells,  
111 such as some cells have typical macrophages morphology including amoeboid shape, largest  
112 surface area and cell volume, while other cells remain as spherical shape during differentiation.  
113 Moreover, highly diverse invaded intracellular bacteria numbers and invasion times were observed  
114 between different macrophages, suggesting distinct degrees of host immune system activation. To  
115 investigate the heterogeneous chromatin architecture of these cells at single cell level, we  
116 developed a single-cell-indexed DLO Hi-C (sciDLO Hi-C) based on DLO Hi-C<sup>20</sup> and two rounds  
117 of molecular barcoding to capture the chromatin conformation of individual cells (**Fig. 1b**). The  
118 advantage of this method is that only the 80 bp DNA fragments containing the proximity ligation  
119 junction were retained, which can greatly reduce the sequencing noise caused by multiple  
120 displacement amplification (**Extended Data Fig. 1d-f and Methods**). By comparing with other

121 single-cell Hi-C methods<sup>4,21,22</sup>, we demonstrated that sciDLO Hi-C data-sets contains the highest  
122 proportion of proximity ligation junction reads<sup>4</sup> (**Extended Data Fig. 1e**).

123

124 By sciDLO Hi-C, we obtained 3D genome data of 409 Thp1-mono cells, 424 Thp1-macro  
125 cells, and 510 Thp1-*M.tb* cells (**Supplementary Table 3**). The territories between different  
126 chromosomes can be clearly distinguished based on the simulated 3D genome structure of the  
127 individual cells (**Extended Data Fig. 1g, h**). Next, the single cell data were merged to generate a  
128 pooled Hi-C matrix, which is similar to the bulk Hi-C data (**Extended Data Fig. 1i**). To investigate  
129 the heterogeneity of these three type of cells, we employed scHiCTools<sup>23</sup> to classify all the  
130 individual cells based on their 3D genome structures. As shown in **Fig. 1c**, three distinct clusters  
131 of cells were identified, representing Thp1-mono, Thp1-macro, and Thp1-*M.tb*, respectively.  
132 Among which, the Thp1-mono has obvious boundaries between the other two types of cells,  
133 whereas Thp1-macro and Thp1-*M.tb* are partially overlapped. This data reflected that PMA  
134 treatment could uniformly reprogram monocyte to a distinct cell type macrophage, whereas  
135 macrophage activation caused by *M.tb* infection was much more heterogeneous. Notably,  
136 compared to Thp1-macro and Thp1-mono cells, Thp1-*M.tb* were enriched with significantly more  
137 chromatin contacts around the immune genes (**Fig. 1d**). For example, the simulated chromatin  
138 structures of individual cells showed that the chromatin interaction between innate immune-related  
139 genes *NOD2* and *BRD7* were more contacted in Thp1-*M.tb* cells (**Fig. 1e,f**).

140

141 **TAD degree of disorder (DoD) represents genome organizational patterns and correlates with**  
142 **gene transcription**

143 To explore the order and stochasticity of genome organization, we further analyzed chromatin  
144 contact patterns in individual cells. We observed that while the individual chromatin contacts  
145 displayed a certain extent of heterogeneity, the chromatin structures in specific regions of a cell  
146 in certain process were uniformly folded. Take the innate immune-related *STAT1* gene locus as an  
147 example (**Fig. 2a-d**). Most of the individual Thp1-macro cells had stochastic chromatin interaction

148 pattern between *STAT1* promoter and an potential enhancer (**Fig. 2a,c and Extended Data Fig.**  
149 **2a**), while the promoter-enhancer contact patterns of Thp1-*M.tb* cells in this region were much  
150 more consistent (**Fig. 2b,d**). These data suggested that in the highly organized genome regions,  
151 there was an intrinsic non-randomness or certainty for chromatin folding at both single cell and  
152 bulk cell level.

153

154 Next, we proposed the concept of TAD degree of disorder (DoD) and developed an algorithm  
155 to measure the order and stochasticity of the genome architecture organization of the individual  
156 cells (**Extended Data Fig. 2b-d and Methods**). As only the high order genome loci with similar  
157 chromatin interaction in individual cells could exhibit significant interaction spots in the merged  
158 Hi-C matrix (**Fig. 2e and Supplementary Table 4**). We retained all the significant interaction  
159 spots in the Hi-C matrix to filter the stochastic genome loci with random chromatin interactions.  
160 As the distance between the spots might reflect the similarity of the chromatin folding patterns,  
161 the overall mean distance between the spots was then calculated to represent the whole DoD value  
162 in the TAD (**Extended Data Fig. 2b**). As shown in **Extended Data Fig. 2e**, the closer spot clusters  
163 could indeed reflect highly organized chromatin folding patterns. Moreover, the DoD can faithfully  
164 indicate the order of the chromatin organization in the individual cells in **Fig. 2a-d**.

165

166 We further calculated the whole genome TAD DoD of the THP-1 cells during differentiation  
167 and infection. As illustrated in **Extended Data Fig. 2f**, the overall TAD DoD distributions in Thp1-  
168 mono, Thp1-macro, and Thp1-*M.tb* suggest a dynamic genome architecture alteration during  
169 differentiation and infection.

170

171 Next, the TAD around MYC gene was used an example to illustrate the detailed DoD  
172 dynamics. As this genome locus with abundant enhancer and suppressor elements around the *MYC*  
173 gene is crucial for cell pluripotency and stemness<sup>24</sup>. In Thp1-mono, the chromatin contacts in this  
174 region were randomly distributed and had no obvious interaction patterns (DoD=2.74). Notably,

175 the Hi-C matrix of this TAD displayed more highly organized chromatin contact patterns  
176 (DoD=2.42) after differentiation (**Fig. 2f**), suggesting a systematic non-random promoter-enhancer  
177 or promoter-repressor<sup>24</sup> interaction occurred in the individual cells during differentiation. Notably,  
178 we observed a stripe structure right above *MYC* gene after differentiation (**Fig. 2f**, marked with  
179 dashed box), which may be attributed to the highly organized chromatin contacts of *MYC* gene to  
180 a series of cis-elements or genes in this TAD.

181

182 Next, we investigated the relationship between the order of the genome architecture  
183 organization and the gene expression level in the TAD. As shown in **Fig. 2g**, the TADs with lower  
184 DoD values have generally higher gene expression level in comparison with the more randomly  
185 organized TADs with higher DoD in all three cell types. Moreover, the high order TADs with lower  
186 DoD values are more enriched in the A compartments, whereas the TADs with higher DoD values  
187 are more enriched in the B compartments (**Fig. 2h**), suggesting the stochasticity of TAD  
188 organization is highly related to gene transcription.

189

190 As low DoD reflects that the individual cells have similar folding patterns and the chromatin  
191 organization is less stochastic, the genes in these TADs may undergo similar transcriptional  
192 regulation. In this scenario, the genes in highly organized (low DoD) TADs may be more likely to  
193 be synchronously coregulated due to the cooperation within the same transcriptional regulatory  
194 complex. To test this hypothesis, we defined the average gene coregulation score (CRS) within a  
195 TAD during differentiation and infection, as shown in **Extended Data Fig. 2g**. Notably, we found  
196 that TADs with lower DoDs had overall higher CRSs (**Fig. 2i**), supporting that highly organized  
197 chromatin tends to be more synchronously (or less randomly) coregulated.

198

199 Our bulk cell Hi-C data demonstrated that the TADs of the THP-1 cells were underwent with  
200 different kind of dynamics during differentiation and infection. Around 30% of TADs changed  
201 their boundaries, including TAD shift, fusion, and division (**Extended Data Fig. 2h**). For the

202 boundaries remained intact TADs, 24.2% of TAD DoDs decreased, and 3.4% increased during cell  
203 differentiation, whereas 12.0% decreased and 5.4% increased during *M.tb* infection (**Extended**  
204 **Data Fig. 2i**). As it has been demonstrated that the TAD boundary dynamic could modulate the  
205 gene transcription inside TADs<sup>25</sup>, we compared the influence of TAD DoD dynamic with other  
206 TAD boundary dynamics on the gene transcription inside the TADs. As shown in **Fig. 2j**, the  
207 dynamic DoD has a more profound influence on gene expression within the TAD than other types  
208 of boundary dynamics, including TAD boundary shift, fusion, and division. These results  
209 supported the functional significance of TAD DoD.

210

### 211 ***Active chromatin marks are enriched in the low DOD chromatin regions***

212 To further investigate the relationship between the organization of genome architecture and  
213 chromatin epigenetic modification, we systematically investigated the epigenetic chromatin states  
214 across Thp1-mono, Thp1-macro, and Thp1-*M.tb* cells by ATAC-Seq and comprehensive ChIP-Seq  
215 with H3K4me3, H3K4me1, H3K27ac, H3K27me3 and H3K9me3 antibodies. The combination of  
216 these analysis revealed the whole genome epigenetic chromatin state and promoter/enhancer state  
217 dynamics of THP-1 cells during differentiation and infection (**Extended Data Fig. 3a-c**).  
218 **Extended Data Fig. 3d** show that the overall gene expression levels are correlated to the promoter  
219 activity epigenetic states, supporting the integrity of the epigenetic analysis. Upon *M.tb* infection,  
220 423 promoters changed from the repressive state to the active state (**Extended Data Fig. 3c and**  
221 **Supplementary Table 5**). The genes harboring these promoters are enriched in several immune  
222 defense pathways (**Extended Data Fig. 3e**), suggesting that *M.tb* infection could convert  
223 macrophages to the active M1 state by systematical epigenetic reprogramming.

224

225 Next, we analyzed the distribution of the active and repressive epigenetic marks in the TADs  
226 with different DoDs. **Fig. 3a** demonstrate that the enhancer and promoter active chromatin marks,  
227 such as H3K4me1, H3K27ac, and H3K4me3, are significantly more enriched in the TADs with  
228 low DoD values. In contrast, TADs with high DoD contain significantly more transcription

229 repressive signals and heterochromatin signals, such as H3K27me3 and H3K9me3 (**Fig. 3b**). Our  
230 data implied that the genome architecture of TADs with low DoDs were more sophisticatedly  
231 organized, which might be mediated by the elegant cooperation with a greater number of  
232 transcriptional regulatory factors and more accessible chromatin within TADs. Consistent with this  
233 hypothesis, we observed that the DoD was indeed highly negatively correlated with ATAC signals  
234 within the TADs (**Fig. 3c**), suggesting that the DoD is correlated to the chromatin accessibility and  
235 the subsequent binding of transcriptional regulatory proteins.

236

237 HERC5 and HERC6 are IFN-induced HECT-type E3 protein ligases involved in anti-bacterial  
238 defense<sup>26</sup>. We observed that the TAD DoD value of HERC5 and HERC6 gene regions were  
239 significantly decreased upon *M.tb* infection, suggesting a refining of the genome architecture  
240 organization (**Fig. 3d,e**). Moreover, the ATAC peak and active chromatin marks such as H3K4me3  
241 and H3K27ac were enriched in the promoter region. Consistently, the expression of HERC5 and  
242 HERC6 were also synchronously co-upregulated (**Fig. 3f,g**). By simulating the spatial structure of  
243 this region, we found that in the low DOD state, the spatial distance between HERC5 and HERC6  
244 was more adjacent (**Fig. 3h,i**), suggesting these two genes have the tendency to cooperate with  
245 each other and be co-regulated by the same transcription regulatory complex in response to the  
246 infection.

247

248 Our bulk and single cell DLO Hi-C data suggested that the TADs with low DoD display a  
249 high degree of certainty and consistence of the local chromatin folding patterns among individual  
250 cells. Thus, the TAD “degree of disorder” may reflect the entropy of the chromatin organization in  
251 a TAD. The highly organized TADs with lower “TAD entropy” levels have overall lower DoD  
252 values, more active enhancer/promoter enrichment, higher gene transcription levels and more  
253 concerted coregulation. In contrast, the disordered TADs with higher “TAD entropy” levels  
254 generally exhibit lower transcription and more random coregulation (**Fig. 3j**). Together, these  
255 results suggested that the order of chromatin structure is highly correlated with its epigenetic

256 modification and gene transcription.

257

258 ***Remodeling of the chromatin configuration around GBP family genes orchestrates their***  
259 ***coexpression upon M.tb infection***

260 To further investigate local TAD DoD in details, we explored the genome sites with dynamic  
261 DoD, such as the TAD with the guanylate binding protein (GBP) gene family, of which the DoD  
262 was significantly decreased upon *M.tb* infection in the bulk cell DLO Hi-C data (**Fig. 4a**). The  
263 single-cell chromatin interaction matrix with high quality in this *GBP* region were merged as  
264 shown in **Fig. 4b**, in which each color represented the chromatin contact from the same individual  
265 cells. We calculated the DoD based on the merged chromatin interaction matrix from sciDLO Hi-  
266 C data and found that the DoD was decreased after *M.tb* infection, which is consistent with the  
267 results from bulk cell Hi-C data.

268

269 By virtue of the merged single cell contact matrix, we found that the chromatin contacts  
270 fluctuate considerably among individual cells, suggesting heterogenous genome organizational  
271 patterns at single cell level. However, upon infection this TAD has smaller DoD and more  
272 intrinsically organized local chromatin interaction patterns in comparison to the random pattern in  
273 the Thp1-macro cells with high DoD (**Fig. 4b**). For example, a series of genome loci in this TAD  
274 were sequentially interacted with *GBP5* respectively among individual Thp1-*M.tb* cells, whereas  
275 the chromatin contact pattern of this location in Thp1-macro cells was much more random (**Fig.**  
276 **4c**). As one Hi-C experiment can only capture chromatin interaction at single time-point, the  
277 merged interactions of *GBP5* with other loci from the individual cells may reflect the chromatin  
278 interactions around *GBP5* from different time-points. As they all looped with *GBP5*, it likely that  
279 these genes are all assembled in a transcription factory.

280

281 Consistent with our observation that DoD is negatively correlated with gene co-regulation,  
282 **Fig. 4a** demonstrated that the expression levels of the *GBP1-5* in the TAD was synchronously co-

283 upregulated. The immunostaining assay showed that GBP family proteins assembled tightly  
284 around the surface of *M.tb* cells probably to prevent its spreading (**Extended Data Fig. 4a**). These  
285 observations may suggest that, in response to *M.tb* infection, this relatively chaotic TAD with high  
286 DoD or entropy became highly organized. This may be coordinated by the opening of specific  
287 genome loci and the subsequent binding of corresponding proteins which formed new chromatin  
288 loops that linked the genes into an active transcription factory. In this way, it could efficiently  
289 achieve synchronous co-transcription of these defense-related genes.

290

291 Transcription factory tends to form liquid-liquid phase separation (LLPS) condensates<sup>27</sup> to  
292 efficiently activate gene transcription. It has been shown that super enhancer (SE) binding protein  
293 MED1 and BRD4 undergo phase separation and can be used as phase separation marker proteins  
294 within transcription factory<sup>28</sup>. We then test whether *GBP* family gene region is relocated into LLPS  
295 zone in the process of immune activation. Based on previous BRD4 and MED1 ChIP-seq data<sup>29</sup>,  
296 we found that GBP family genome region were enriched with these two phase separation marker  
297 proteins (**Fig. 4d**). Our ATAC-seq and H3K4me3 ChIP-seq data indicate that the chromatin state  
298 is activated and may bind with more regulatory proteins after infection (**Fig. 4a**). Furthermore, the  
299 integrated Hi-C chromatin loop and BRD4 and MED1 ChIP-seq analysis suggest that the BRD4  
300 and MED1 occupied SE are spatially in close proximity to all the GBP family gene loci after *M.tb*  
301 infection (**Fig. 4d**).

302

303 To further confirm phase separation in GBP gene family region, we performed co-staining of  
304 BRD4 and MED1 (by Immunofluorescence) with GBP gene family region (by fluorescence in situ  
305 hybridization). As shown in **Fig. 4e** and **Extended Data Fig. 4b**, the overlapping ratio of BRD4  
306 and MED1 puncta and the DNA-FISH signal of GBP gene family region is significantly increased  
307 after infection, suggesting the *GBPs* region tends to relocate into LLPS transcription factory zone  
308 to efficiently initiate these immune-defense gene expression. Together, our data implied that  
309 macrophages could dynamically adapt their 3D genome structure and coordinate with LLPS

310 transcription factory to efficiently express these immune-defense gene to fulfil distinct  
311 physiological functions during immunological response.

312

313 ***NF-κB initiates systematic chromatin remodeling of its target genome regions during M.tb***  
314 ***infection***

315 During differentiation and *M.tb* infection, the overall DoD were gradually decreased, which  
316 is in line with the plasticity of these cells (**Fig. 5a** and **Extended Data Fig. 5a**). In these processes,  
317 the reduction of DoD was accompanied with the increase of chromatin loops, suggesting that more  
318 loop mediated cis-element interaction occurs in low DoD region (**Fig. 5b**). Upon infection, about  
319 1,864 loops were strengthened. These chromatin loops related genes are listed in **Supplementary**  
320 **Table 6**. Notably, these genes are significantly enriched in immunity pathways, which is not  
321 observed in the genes located in the weakened loops (**Extended Data Fig. 5b**). The dynamic  
322 immunity related enhancer-gene regulatory network in Chr12 during infection was shown in  
323 **Extended Data Fig. 5c**. The KEGG analysis of strengthened loop anchor genes (**Supplementary**  
324 **Table 6**) showed that, 5 of the top 10 enriched pathways were directly related to NF-κB signaling  
325 pathways (**Extended Data Fig. 5d**). Furthermore, a large number of NF-κB binding motifs were  
326 enriched around the transcription start site (TSS) of these strengthened loop anchor genes (**Fig.**  
327 **5c**), suggesting that NF-κB participates in chromatin remodeling during *M.tb* infection. The  
328 immunofluorescence assay revealed that NF-κB (p65) was indeed translocated into the nucleus  
329 upon infection (**Fig. 5d**).

330

331 The chromatin accessibility and RNA expression analysis showed that, upon *M.tb* infection,  
332 the NF-κB target loci turned to be more open and the expression level of target genes was  
333 significantly up-regulated compared to the random genes (**Fig. 5e**). Moreover, the chromatin loops  
334 related to the NF-κB target genes were more strengthened compared to the random genes (**Fig. 5f**).  
335 We further investigated the chromatin remodeling of the typical NF-κB target gene loci, such as  
336 *IFITs*, *CCLs*, *GBPs*, *HERCs*, *NFKB1*, and *TNFSF10*. **Fig. 5g** demonstrated that upon infection, a

337 greater number of loops were formed in these regions and the corresponding DoD was also reduced.  
338 This data was further validated by ChIP-PCR, showing that the NF- $\kappa$ B was significantly enriched  
339 in the loop anchor regions of *IFIT3*, *CCL2*, *GBP4*, and *HERC2* upon infection (**Extended Data**  
340 **Fig. 5e**). These evidences suggest that, upon infection, NF- $\kappa$ B translocated into nucleus, bound to  
341 specific target regions, readjusted the local DoD by reorganizing the chromatin structure for a  
342 concerted transcription of the defense genes.

343

344 *IFIT* gene loci are NF- $\kappa$ B target gene sites<sup>30</sup>, of which the DoD was decreased upon infection.  
345 The single cell Hi-C data also demonstrated that the local chromatin interaction pattern became  
346 more ordered during infection (**Fig. 5h**). The chromatin loop analysis revealed that these *IFIT*  
347 genes were regulated by a single upstream cis element enriched with NF- $\kappa$ B binding motif (**Fig.**  
348 **5i,j**). Before infection, the cis-element was linked to *IFIT1B* and *IFIT5* (**Fig. 5i**), which were  
349 dynamically reshuffled to link with *IFIT1*, *IFIT2*, and *IFIT3* after infection (**Fig. 5j**). Interestingly,  
350 it has been demonstrated that IFIT1, IFIT2, and IFIT3 proteins can interact with each other and  
351 form a complex to perform antipathogenic functions<sup>31</sup>. Consistently, we observed synchronously  
352 upregulated expression of these three genes in the newly established loops (**Fig. 5j**). Notably,  
353 *IFIT1B* and *IFIT5*, which are not located in this spatially adjacent hub, were not upregulated. These  
354 data demonstrated a high order chromatin structure mediated elegant spatial and temporal co-  
355 regulation of the NF- $\kappa$ B target genes transcription during immunoresponse (**Fig. 5k**).  
356

### 357 *A remote NF- $\kappa$ B enriched enhancer promotes the expression of PD-L1 through chromatin loop*

358 After engulfing *M.tb*, macrophages can present *M.tb* antigens via major histocompatibility  
359 complex (MHC) molecules to T-cells to eliminate *M.tb* infection<sup>32</sup>. During this process, *M.tb* also  
360 evolves various strategies to escape immunological clearance. In this scenario, we observed  
361 immune checkpoint protein PD-L1, which can counteracting T cell-activating signals, was  
362 dramatically upregulated after *M.tb* infection (**Extended Data Fig. 1c**). Through the Hi-C contact  
363 matrix, we identified a putative enhancer region highly enriched with H3K4me3 modification

364 (Chr9: 4,760,070-4,769,779) contact with the PD-L1 promoter through a Hi-C loop (**Fig. 6a-c**).  
365 Notably, the ATAC-seq data showed that these enhancer and promoter regions were more  
366 accessible and enrichment active chromatin modifications after *M.tb* infection (**Fig. 6b,c**),  
367 indicates that more regulatory proteins are enriched in the enhancer region. Transcription factor  
368 binding motif analysis revealed that both enhancer and promoter (**Fig. 6b,c and Extended Data**  
369 **Fig. 6a,b**) regions can be bound by NF- $\kappa$ B. What's more, by ChIP-qPCR, we proved that NF- $\kappa$ B  
370 (p65) was significantly enriched in this enhancer region after infection (**Fig. 6d**).  
371

372 Since NF- $\kappa$ B can directly induces *PD-L1* gene transcription by binding to its promoter<sup>33</sup>, we  
373 speculate that this enhancer region can directly regulate the *PD-L1* gene expression mediated by  
374 chromatin loop. To further confirm the function of PD-L1 enhancer, we knocked out this enhancer  
375 region in the THP-1 cell line by the CRISPR/Cas9 system and validated its regulatory function  
376 (**Fig 6e and Extended Data Fig. 6c-f**). As predicted, the qPCR and western blot data demonstrated  
377 that knockout of the *PD-L1* enhancer can indeed attenuate the upregulation of PD-L1 expression  
378 at both mRNA and protein levels upon *M.tb* infection (**Fig. 6f,g**). Collectively, these results  
379 suggested a synchronous opening of the enhancer and promoter regions for transcription factor  
380 binding and activated *PD-L1* gene transcription during *M.tb* infection (**Fig. 6h**). This PD-L1  
381 enhancer has potential to become anti-tuberculosis and even anti-tumor therapeutic target. It would  
382 be of great interest to further investigate how *M.tb* infection reprogram the epigenetic code in this  
383 enhancer locus and what is physiological role of this modification in the pathogenesis of *M.tb*.  
384

385 ***Integrated omics analysis of long-range target genes of TB susceptibility loci via chromatin***  
386 ***looping***

387 To obtain a comprehensive map of tuberculosis (TB) susceptibility loci and their long-  
388 range regulatory gene targets via chromatin looping, we collected all reported TB susceptibility  
389 loci<sup>14-17</sup> and performed integrated omics analysis of GWAS, eQTL, and Hi-C (**Fig. 7a, Extended**  
390 **Data Fig. 7a, and Supplementary Table 7**). The comprehensive TB susceptibility loci and their

391 target genes through long-range chromatin interactions were shown in **Extended Data Fig. 7b**. Of  
392 note, the chromatin interaction loops between the *LRRK2*, *NSL1*, and *ASAPI* and the  
393 corresponding TB susceptibility loci were significantly strengthened during *M.tb* infection (**Fig.**  
394 **7b** and **Extended Data Fig. 7c,d**). Importantly, the target genes of TB susceptibility loci  
395 discovered by this integrated omics analysis, such as *ASAPI* and *LRRK2*, have been reported to be  
396 involved in TB pathogenesis<sup>17,34</sup>, supporting the integrity of our multiomics analysis.  
397

398 We further analyzed *LRRK2*, which has a strong loop and eQTL correlation with the TB  
399 susceptibility SNP rs1873613. The DoD in the TAD was decreased after *M.tb* infection (**Fig. 7b**).  
400 Moreover, the simulated chromatin structure revealed that SNP rs1873613 and *LRRK2* tended to  
401 be adjacent in space upon infection (**Fig. 7c**). The ENCODE ChIP-Seq data showed that this SNP  
402 is located in the enhancer region of *LRRK2* with the binding site of STAT3, SPI1, and FOS  
403 (**Extended Data Fig. 7e**). Moreover, this SNP is located right in the anchor of an *LRRK2* chromatin  
404 loop that was significantly strengthened after infection (**Fig. 7b**). This data suggests that this TB  
405 susceptibility SNP locus was dynamically reshuffled upon infection to spatially link with *LRRK2*  
406 to regulate its gene transcription. Consistently, the eQTL analysis data showed that a T:C mutation  
407 can indeed increase the expression of *LRRK2* in the lungs (**Fig. 7d**). This SNP in the patient may  
408 possibly influence the contact of *LRRK2* and the enhancer and therefore disturb the transcription  
409 regulation of *LRRK2*.

410

411 It has been demonstrated that LRRK2 promoted the proliferation of *M.tb* by inhibiting  
412 phagosomes maturation<sup>34</sup>, suggesting LRRK2 might be a TB drug target. Thus, we investigated  
413 the anti-*M.tb* effect of AdoCbl, an inhibitor of LRRK2<sup>35</sup>. As shown in **Fig. 7e-g**, AdoCbl can indeed  
414 promote the maturation of phagosomes in TB-infected bone marrow-derived macrophages and  
415 decrease the colony-forming unit count of intracellular *M.tb*. Furthermore, the *in vivo* experiment  
416 showed that AdoCbl could significantly inhibit the proliferation of *M.tb* in the lungs (**Fig. 7h,i**).  
417 This result was further supported by hematoxylin-eosin staining of tissue sections, showing that

418 AdoCbl significantly inhibited the initiation of lung and spleen lesions (**Fig. 7j**). These data  
419 revealed that the TB susceptibility SNP (rs1873613) in the dynamic anchor of *LRRK2* enhancer  
420 loop could promote the expression of *LRRK2* through chromatin looping. It subsequently  
421 represses the clearance of *M.tb* by inhibiting phagosome maturation and thus causes susceptibility  
422 to TB, of which this process can be attenuated by a potential TB drug candidate, AdoCbl  
423 (**Extended Data Fig. 7f**).

424

425 Collectively, we delineated the 4D genome landscape of THP-1 cells during differentiation  
426 and infection at single cell resolution. Our data showed that the immunological enhancer-promoter  
427 loops, especially the NF- $\kappa$ B target regions, were reorganized to orchestrate synchronous defense  
428 gene transcription for *M.tb* clearance. It provides a comprehensive resource for epigenetic  
429 regulation of immunocytes and for *M.tb* infection studies, such as anti-*M.tb* drug screening and  
430 the TB pathogenesis mechanisms of the patients with susceptibility SNPs. Importantly, we  
431 proposed TAD DoD to measure the genome organizational patterns, which is correlated with the  
432 chromatin epigenetic states, chromatin structure variability in individual cells, expression and co-  
433 regulation of the genes within the TAD, supporting the order and stochasticity of genome  
434 architecture is related to its function. These data shed insights into the dynamic genome  
435 organizational patterns at single cell level and illustrated how the 4D genome coordinates gene  
436 transcriptional programs during differentiation or in response to different stimulus.

437

438 **References**

- 439 1. Schrodinger, E. What is life? The physical aspect of the living cell. (At the University Press,  
440 1951).
- 441 2. Misteli, T. Beyond the sequence: cellular organization of genome function. *Cell* **128**, 787-  
442 800 (2007).
- 443 3. Rowley, M.J. & Corces, V.G. Organizational principles of 3D genome architecture. *Nature  
444 Reviews Genetics* **19**, 789-800 (2018).
- 445 4. Ulianov, S.V. et al. Order and stochasticity in the folding of individual Drosophila genomes.  
446 *Nature Communications* **12**, 1-17 (2021).
- 447 5. Kanherkar, R.R., Bhatia-Dey, N. & Csoka, A.B. Epigenetics across the human lifespan.  
448 *Front. Cell Dev. Biol.* **2**, 49 (2014).
- 449 6. Meissner, A. Epigenetic modifications in pluripotent and differentiated cells. *Nat.  
450 Biotechnol.* **28**, 1079–1088 (2010).
- 451 7. Misteli, T. The Self-Organizing Genome: Principles of Genome Architecture and Function.  
452 *Cell* (2020).
- 453 8. Mourad, R. & Cuvier, O. Predicting the spatial organization of chromosomes using  
454 epigenetic data. *Genome Biol.* **16**, 182 (2015).
- 455 9. Garg, S.K., Vitvitsky, V., Gendelman, H.E. & Banerjee, R. Monocyte differentiation,  
456 activation, and mycobacterial killing are linked to transsulfuration-dependent redox  
457 metabolism. *J. Biol. Chem.* **281**, 38712–38720 (2006).

- 458 10. Skinner, B.M. & Johnson, E.E. Nuclear morphologies: their diversity and functional  
459 relevance. *Chromosoma* **126**, 195–212 (2017).
- 460 11. Ivashkiv, L.B. Epigenetic regulation of macrophage polarization and function. *Trends*  
461 *Immunol.* **34**, 216–223 (2013).
- 462 12. World Health Organization Global Tuberculosis Report 2018. (World Health Organization,  
463 Geneva; 2018).
- 464 13. Shi, C. & Pamer, E.G. Monocyte recruitment during infection and inflammation. *Nat. Rev.*  
465 *Immunol.* **11**, 762–774 (2011).
- 466 14. Thye, T. et al. Genome-wide association analyses identifies a susceptibility locus for  
467 tuberculosis on chromosome 18q11.2. *Nat. Genet.* **42**, 739–741 (2010).
- 468 15. Thye, T. et al. Common variants at 11p13 are associated with susceptibility to tuberculosis.  
469 *Nat. Genet.* **44**, 257–259 (2012).
- 470 16. Zheng, R. et al. Genome-wide association study identifies two risk loci for tuberculosis in  
471 Han Chinese. *Nat. Commun.* **9**, 4072 (2018).
- 472 17. Curtis, J. et al. Susceptibility to tuberculosis is associated with variants in the ASAP1 gene  
473 encoding a regulator of dendritic cell migration. *Nat. Genet.* **47**, 523–527 (2015).
- 474 18. Phanstiel, D.H. et al. Static and dynamic DNA loops form AP-1-bound activation hubs  
475 during macrophage development. *Mol. Cell* **67**, 1037–1048.e1036 (2017).
- 476 19. Auwerx, J. The human leukemia cell line, THP-1: a multifaceted model for the study of  
477 monocyte-macrophage differentiation. *Experientia* **47**, 22–31 (1991).

- 478 20. Lin, D. et al. Digestion-ligation-only Hi-C is an efficient and cost-effective method for  
479 chromosome conformation capture. *Nat. Genet.* **50**, 754–763 (2018).
- 480 21. Flyamer, I.M. et al. Single-nucleus Hi-C reveals unique chromatin reorganization at  
481 oocyte-to-zygote transition. *Nature* **544**, 110-114 (2017).
- 482 22. Tan, L., Xing, D., Chang, C.-H., Li, H. & Xie, X.S. Three-dimensional genome structures  
483 of single diploid human cells. *Science* **361**, 924-928 (2018).
- 484 23. Li, X., Feng, F., Leung, W.Y. & Liu, J. scHiCTools: a computational toolbox for analyzing  
485 single-cell Hi-C data. *bioRxiv*, 769513 (2020).
- 486 24. Fulco, C.P. et al. Systematic mapping of functional enhancer–promoter connections with  
487 CRISPR interference. *Science* **354**, 769-773 (2016).
- 488 25. Arzate-Mejía, R.G., Cerecedo-Castillo, A.J., Guerrero, G., Furlan-Magaril, M. & Recillas-  
489 Targa, F. In situ dissection of domain boundaries affect genome topology and gene  
490 transcription in Drosophila. *Nature communications* **11**, 1-16 (2020).
- 491 26. Wong, J.J.Y., Pung, Y.F., Sze, N.S.-K. & Chin, K.-C. HERC5 is an IFN-induced HECT-  
492 type E3 protein ligase that mediates type I IFN-induced ISGylation of protein targets.  
493 *Proceedings of the National Academy of Sciences* **103**, 10735-10740 (2006).
- 494 27. Palikyras, S. & Papantonis, A. Modes of phase separation affecting chromatin regulation.  
495 *Open biology* **9**, 190167 (2019).
- 496 28. Sabari, B.R. et al. Coactivator condensation at super-enhancers links phase separation and  
497 gene control. *Science* **361** (2018).

- 498 29. Angus, S.P. et al. FOXA1 and adaptive response determinants to HER2 targeted therapy in  
499 TBCRC 036. *NPJ breast cancer* **7**, 1-15 (2021).
- 500 30. Xu, F. et al. NF-κB-dependent IFIT3 induction by HBx promotes Hepatitis B virus  
501 replication. *Frontiers in microbiology* **10**, 2382 (2019).
- 502 31. Fleith, R.C. et al. IFIT3 and IFIT2/3 promote IFIT1-mediated translation inhibition by  
503 enhancing binding to non-self RNA. *Nucleic Acids Res.* **46**, 5269–5285 (2018).
- 504 32. Harding, C.V. & Boom, W.H. Regulation of antigen presentation by mycobacterium  
505 tuberculosis: a role for toll-like receptors. *Nat. Rev. Microbiol.* **8**, 296–307 (2010).
- 506 33. Antonangeli, F. et al. Regulation of PD-L1 Expression by NF-κB in Cancer. *Frontiers in*  
507 *immunology* **11** (2020).
- 508 34. Härtlova, A. et al. LRRK2 is a negative regulator of *Mycobacterium tuberculosis*  
509 phagosome maturation in macrophages. *EMBO J.* **37**, e98694 (2018).
- 510 35. Schaffner, A. et al. Vitamin B12 modulates Parkinson's disease LRRK2 kinase activity  
511 through allosteric regulation and confers neuroprotection. *Cell Res.* **29**, 313–329 (2019).
- 512
- 513

514 **Materials and Methods**

515 ***Cell culture and mycobacterial infection***

516 THP-1 cells (ATCC, TIB-202) were grown in RPMI-1640 containing 10 % FBS. To differentiate  
517 the monocytes to macrophages, cells were treated with PMA (phorbol 12-myristate 13-acetate)  
518 (final concentration = 40 ng/μl) for 48 h at 37 °C in a 5% CO<sub>2</sub> atmosphere, and then washed with  
519 pre-warmed PBS and incubated with fresh culture medium for another 24 h. For *M.tb* infection  
520 experiment, H37Ra was pelleted (4,000 rpm, RT, 10 min), washed twice with RPMI-1640,  
521 resuspended in 1 ml THP-1 culture medium, and dispersed using BD insulin syringes (BD,  
522 328421). Monocyte derived macrophages (Thp1-macro) were infected with H37Ra at MOI  
523 (multiplicity of infection) 20. Four hours later the infected cells were washed twice with pre-  
524 warmed PBS and incubated with fresh culture medium for another 8 h.

525

526 ***RNA-Seq library preparation***

527 RNA was extracted using the RNAiso Plus (Takara, 9109) according to manufacturer's protocol.  
528 Sequencing libraries were prepared using the VAHTS Stranded mRNA-Seq Library Prep Kit  
529 (Vazyme, NR602-02) according to manufacturer's protocol.

530

531 ***ChIP-Seq library preparation***

532 4×10<sup>6</sup> cells and 3 μg antibody were used per immunoprecipitation. Antibody of H3K4me1 (Abcam,  
533 ab8895), H3K4me3 (Abcam, ab8580), H3K9me3 (Abcam, ab8898), H3K27ac (Abcam, ab4729),  
534 and H3K27me3 (Millipore, 07-449) were used in this study. The ChIP DNA was obtained using  
535 SimpleChIP® Enzymatic Chromatin IP Kit (CST, #9003). After immunoprecipitation, ChIP-seq  
536 library was constructed using NEBNext® Ultra™ DNA Library Prep Kit (NEB, E7370S).

537

538 ***ATAC-Seq library preparation***

539 1×10<sup>5</sup> cells were centrifuged at 800 g for 5 min and then washed once using 500 μl of cold 1× PBS  
540 and centrifuged at 800 g for another 5 min. Cells were lysed using cold lysis buffer (10 mM Tris-

541 HCl (pH 8.0 at 25 °C), 10 mM NaCl, 0.3% Igepal CA-630). After lysis, nuclei were spun down at  
542 800g in 4 °C for 10 min. The pellet was resuspended in the transposase reaction mix (10 µl 5×  
543 TTBL buffer (Vazyme, TD501-02), 5 µl TTE Mix V50 buffer (Vazyme, TD501-02) and 35 µl  
544 ddH<sub>2</sub>O water). Tagmentation was carried out for 10 min at 55 °C. Immediately following  
545 transposition, the DNA was purified using a Qiagen MinElute PCR Purification Kit (Qiagen,  
546 28004) and eluted with 10 µl elution buffer. The ATAC-Seq library was amplified by the primers  
547 in TruePrepTM Index Kit V2 for Illumina® (Vazyme, TD202).

548

549 ***In situ DLO Hi-C experiment***

550 *In situ* DLO Hi-C was performed as previously described <sup>20</sup>. Five million cells were double cross-  
551 linked with 1.5 mM EGS (Thermo) and 1% formaldehyde (Sigma) and lysed in lysis buffer (10  
552 mM Tris-HCl (pH 8.0 at 25 °C), 10 mM NaCl, 0.3% Igepal CA-630, 0.5% SDS, and complete  
553 protease inhibitor (Roche)), incubated at 60 °C for 5 min, and placed on ice immediately. After  
554 incubation, the nuclei were pelleted by centrifugation at 1,000 r.p.m. for 5 min and washed them  
555 once with ice-cold PBS. A total of 310 µl of ddH<sub>2</sub>O, 20 µl of 20% Triton X-100, 40 µl of 10×  
556 NEBuffer 2.1, and 30 µl of MseI (NEB, 10 units/µl) was then added to the nuclei and incubated  
557 for 6 h at 37 °C with rotation at 15 r.p.m. After restriction enzyme digestion, 50 µl of MseI half  
558 linkers (600 ng/µl), 5 µl of 100 mM ATP, 20 µl of T4 DNA ligase (Thermo, 5 units/µl), and 25 µl  
559 of ddH<sub>2</sub>O were added to the 400 µl of digested chromatin and mixed thoroughly. The mixture was  
560 then incubated at 25 °C for 1 h with rotation at 15 r.p.m. After half-linker ligation, the nuclei were  
561 centrifuged at 4 °C for 5 min at 1000 r.p.m. and washed twice with 1 ml of ice-cold PBS. The  
562 linker-ligated nuclei were gently resuspended in 200 µl of 1× T4 DNA ligation buffer (Thermo)  
563 containing 0.5 units/µl T4 polynucleotide kinase (NEB) and incubated at 37 °C for 30 min. The  
564 200-µl reaction complexes were added to 300 µl of 1× T4 DNA ligation buffer (Thermo)  
565 containing 0.5 units/µl T4 DNA ligase (Thermo). Ligation was performed at 20 °C for 2 h with  
566 rotation at 15 r.p.m. The nuclei were centrifuged at 4 °C for 5 min at 1,000 r.p.m. and resuspended  
567 in 400 µl of ddH<sub>2</sub>O. Protein digestion was performed by adding 25µl of 10 mg/ml proteinase K

568 (Sigma), 50 $\mu$ l of 10% SDS, and 25 $\mu$ l of 5 M NaCl, and the tubes were incubated for 2 h at 65 °C.  
569 After incubation, an equal volume of phenol:chloroform:isoamyl alcohol (25:24:1) was added to  
570 the sample, shaken vigorously, and then centrifuged for 10 min at 14,000 r.p.m. Next, the  
571 supernatant was transferred to a new tube. This process was repeated twice. DNA was precipitated  
572 at room temperature with 5 $\mu$ l of Dr. GenTLE Precipitation Carrier (Takara), 50 $\mu$ l of 3 M sodium  
573 acetate (pH 5.2), and 555  $\mu$ l of isopropanol. The precipitated DNA was washed once with 80%  
574 ethanol and dissolved in 160  $\mu$ l of ddH<sub>2</sub>O. A total of 20  $\mu$ l of 10 $\times$  CutSmart buffer, 10  $\mu$ l of SAM  
575 (NEB), and 10  $\mu$ l of MmeI (NEB; 2 units/ $\mu$ l) was added to the 160- $\mu$ l DNA sample, and digestion  
576 was performed at 37 °C for 1 h. The digested DNA sample was subjected to electrophoresis in  
577 native PAGE gels. The specific 80-bp DLO Hi-C DNA fragments were excised and transferred to  
578 a 0.6-ml tube with a pierced bottom. This tube was then placed into a 1.5-ml tube, and the gel  
579 slices were shredded by centrifugation at 14,000 r.p.m. for 10 min. A total of 400  $\mu$ l of TE buffer  
580 was added to the 1.5-ml tube (to ensure that the shredded gel was fully immersed in buffer), and  
581 the mixture was incubated for 20 min at -80 °C, followed by a 2-h incubation at 37 °C with rotation  
582 at 15 r.p.m. Next, the shredded gel, along with the buffer, was transferred into the filter cup of a 2-  
583 ml Spin-X tube filter (Costar, 8160). After centrifugation, the eluate was transferred into a new 2-  
584 ml tube. A total of 4 $\mu$ l of Dr. GenTLE Precipitation Carrier (Takara, 9094), 40 $\mu$ l of 3 M sodium  
585 acetate (pH 5.2), and an equal volume of isopropanol was added to precipitate the DNA. The  
586 precipitated DNA was washed once with 80% ethanol and dissolved in 40  $\mu$ l of ddH<sub>2</sub>O. Next, 1.5  
587  $\mu$ l of PE-adaptor1 (500 ng/ $\mu$ l), 1.5  $\mu$ l of PE-adaptor2 (500 ng/ $\mu$ l), 5  $\mu$ l of 10 $\times$  T4 DNA ligase buffer,  
588 and 2  $\mu$ l of T4 DNA ligase (Thermo, EL0012) were added to the 40  $\mu$ l of DLO Hi-C DNA  
589 fragments and incubated at 16 °C for approximately 30 min. 90 $\mu$ l of AMPure XP beads (Beckman,  
590 A63880) was added to the ligation mixes and washed twice with 80% ethanol to remove excess  
591 Illumina sequencing adaptors. Next, 45  $\mu$ l of ddH<sub>2</sub>O was used to wash DNA from the beads. The  
592 eluted DNA was repaired using PreCR Repair Mix (NEB, M0309S) for 20 min at 37 °C in a final  
593 volume of 50  $\mu$ l. 5-10  $\mu$ l of repaired DNA was used as a template and amplified for fewer than 13  
594 cycles. The PCR product is the final DLO Hi-C sequencing library.

595 ***Single cell DLO Hi-C experiment***

596 ***1. Nuclei preparation***

597 Five million cells were cross-linked with 1% formaldehyde (Sigma) for 10 mins, and lysed in lysis  
598 buffer (10 mM Tris-HCl (pH 8.0 at 25 °C), 10 mM NaCl, 0.3% Igepal CA-630, 0.5% SDS, and  
599 complete protease inhibitor (Roche)) at 60 °C for 5 min, and placed on ice immediately. After  
600 incubation, the nuclei were pelleted by centrifugation at 1,000 r.p.m. for 5 min and washed once  
601 with nuclei wash buffer (PBS which contain 0.5% Triton X-100, 0.05% Tween 20, and 0.05%  
602 CA630).

603 ***2. MseI digestion***

604 The digestion buffer (a total of 310 µl of ddH<sub>2</sub>O, 20 µl of 20% Triton X-100, 40 µl of 10× NEBuffer  
605 2.1, and 30 µl of MseI (NEB, 10 units/µl)) was then added to the nuclei pellet and digested for 3 h  
606 at 37 °C in thermomixer (Eppendorf) with rotation at 1000 r.p.m.

607 ***3. Indexed half linker ligation***

608 After digestion, 560 µl 2.1x T4 DNA ligase buffer were added to the nuclei, and divided into 96-  
609 well plates and adjusted to the volume of 10 µl/tube. Next, 1 µl barcoded half linkers (50 µM/µl)  
610 (**Supplementary Table 8**) were added to each tube and mixed well. After incubation at room  
611 temperature for 5 min, 1 µl T4 DNA ligase (Thermo, 5 units/µl) were added to each tube. The  
612 ligation reaction was performed at 20 °C for 30 mins, and then incubated for 10 minutes at 4 °C.  
613 The sample in 96-well plates were transferred to 1.5 ml DNA LoBind Tube (Eppendorf,  
614 B148089M), centrifuged at 1,000 r.p.m. for 5 min in 4 °C, and washed 4 times with nuclei wash  
615 buffer.

616 ***4. Fragment-end phosphorylation and in situ proximity ligation***

617 The linker-ligated nuclei were gently resuspended in 200 µl of 1× T4 DNA ligation buffer (Thermo)  
618 containing 0.5 units/µl T4 polynucleotide kinase (NEB) and then incubated at 37 °C for 30 min.  
619 The 200-µl reaction complexes were added to 300 µl of 1× T4 DNA ligation buffer (Thermo)  
620 containing 0.5 units/µl T4 DNA ligase (Thermo). Ligation was performed at 20 °C for 2 h with  
621 rotation at 15 r.p.m. The nuclei were centrifuged at 4 °C for 5 min at 1,000 r.p.m. and resuspended

622 in nuclei wash buffer.

623 **5. Single cell selection and multiple displacement amplification**

624 The nuclei were stained by DAPI (Thermo) and diluted by nuclei wash buffer. The density of  
625 nucleus in liquid was carefully checked under the fluorescence microscope, and adjust to 30  
626 nuclei/ $\mu$ l. Next, about 1  $\mu$ l nuclei were digested with proteinase K to release the DNA, the reaction  
627 system is as follows: 8  $\mu$ l ddH<sub>2</sub>O, 2  $\mu$ l 10x Phi29 MAX DNA Polymerase Reaction Buffer (Vazyme,  
628 N106), 5  $\mu$ l 5N random primer (100  $\mu$ M), 2  $\mu$ l dNTP (10 mM each), 1  $\mu$ l nuclei (~30 nuclei/ $\mu$ l),  
629 and 1  $\mu$ l proteinase K (20 mg/ml). The reaction was performed at 60 °C for 1 hour, 98 °C for 10  
630 min, and 4 °C for 5 min. After proteinase K digestion, 1  $\mu$ l Phi29 MAX DNA Polymerase (Vazyme,  
631 N106) was added to the sample, mixed well and incubated in 30 °C for 3 hours.

632 **6. Multiple displacement amplification recycle and sequencing library construction**

633 After multiple displacement amplification (MDA) reaction, 1  $\mu$ l 10% SDS and 79  $\mu$ l ddH<sub>2</sub>O were  
634 added to the sample, and the DNA was purified by 200  $\mu$ l VAHTS DNA Clean Beads (Vazyme,  
635 N411-01). The following steps of MmeI digestion, 80bp contact DNA fragment recovery are the  
636 same as *in situ* DLO Hi-C protocol described above. For sequencing library construction, we  
637 replaced the previous Illumina sequencing adapter with homemade MGI-2000 platform  
638 sequencing adapter with a second round of indexes (Supplementary information, Fig. S3c and  
639 Table S8). Previous similar methods<sup>36,37</sup> have shown that due to the number of barcodes (96  $\times$  14)  
640 far more than the number of nuclei (30  $\times$  14), therefore most of single nuclei are labeled by a  
641 unique barcodes.

642

643 **DNA-FISH**

644 The primary hybridization probes contain target sequence and readout sequence<sup>38</sup>. Different  
645 groups of probes containing 70 nt target sequences complementary to the genomic region of  
646 interest (around 50 kb) were designed using OligoMiner software<sup>39</sup>. Each group of probes shared  
647 a unique 25-nt readout sequence complementary to the readout probes. All the probes contain more  
648 than 18-nt homology to the repetitive sequences from Repbase were filtered out for specificity<sup>40</sup>.

649 The primary probe loci for GBP2 is chr1:89320076-89370076, and for GBP5 is chr1:89817874-  
650 89867874.

651 DNA FISH was performed following Fast FISH protocol with a little modifications<sup>41</sup>. The  
652 cells were fixed with 4 % formaldehyde solution (Sigma, 47608-250ML-F) at room temperature  
653 for 5 min followed by PBS buffer washing for three times. Cell membrane and nucleus membrane  
654 were permeabilized by methanol incubation for 5 min followed by PBS buffer washing. Next, the  
655 cells were incubated in 0.1 M HCL for 5 mins. After incubation, the cells were heated on a hot  
656 plate at 82 °C for 10 min in 80 % formamide (Sigma) and 2×SSC for DNA denaturation. After  
657 denaturation, cells were incubated for 12 hours in hybridization solution with 2 µM primary  
658 hybridization probes in the presence of 50 % formamide, 8% dextran sulfate sodium salt (Sigma),  
659 and 2× SSC followed by PBS buffer washing for three times. The cells were then incubated for 30  
660 min in a second hybridization solution with 1 µM readout probes in the presence of 30%  
661 formamide and 2×SSC followed by PBS buffer washing for three times and 30% formamide and  
662 2×SSC washing for 3 times. Next, the slides were stained with DAPI (Life Technologies) and  
663 observed under super-resolution microscope (Nikon, N-SIM).

664

#### 665 ***Immunofluorescence combined with DNA-FISH***

666 Cells grown on coated glass were fixed in 4 % formaldehyde solution (Sigma, 47608-250ML-  
667 F) at room temperature for 5 min followed by PBS buffer washing for three times. Next, cells were  
668 permeabilized with 0.4 % SDS in PBS for 5 min at RT. Following three washes in PBS for 5 min,  
669 cells was blocked in blocking buffer (1× PBS/ 5% normal serum / 0.3% Triton X-100) for 60 min.  
670 After blocking, antibodies (anti-BRD4, Abcam ab128874; anti-MED1, Abcam ab64965) in  
671 antibody dilution buffer (1× PBS / 1% BSA / 0.3% Triton X-100) at 2 µg/ml final concentration  
672 were incubated with the slides overnight at 4 °C. Slides were then washed three times with PBS  
673 and recognized by secondary antibodies (Goat antiRabbit IgG Alexa Fluor 488, Life Technologies  
674 A11008, 1:1000 dilution) in the dark for 30 min.

675 After immunofluorescence, cells were placed in prewarmed PBS and incubated at 60 °C for

676 20 min, then incubated in 70% ethanol, 85% ethanol and then 100% ethanol for 1min at RT. After  
677 alcohol dehydration, the cells were heated on a hot plate at 82 °C for 10 min in 80 % formamide  
678 (Sigma) and 2×SSC for DNA denaturation. Next, cells were incubated for 12 hours in  
679 hybridization solution with 2  $\mu$ M Alex555-dUTP labeled *GBP* DNA FISH probes (Chr1:  
680 89,448,890- 89,739,345, Spatial FISH Co. Ltd.) in the presence of 50 % formamide, 8% dextran  
681 sulfate sodium salt (Sigma), and 2× SSC. After hybridization the cells were washing for three times  
682 with 30% formamide and 3 times with 2×SSC. Next, the slides were stained with DAPI (Life  
683 Technologies) and observed under super-resolution microscope (Nikon, N-SIM).

684

#### 685 ***CFU assays***

686 Bone-marrow-derived macrophage cells (BMDM) were seeded into 6-well plate ( $1 \times 10^5$ /well)  
687 and infected with H37Ra at MOI (multiplicity of infection) 20. Four hour later, the infected cells  
688 were washed twice with pre-warmed PBS and incubated with fresh culture medium. Then the cells  
689 were treated with AdoCbl (Sigma, Cat# C0884) at final concentration of 200 $\mu$ M. The PBS solution  
690 used as a negative control. 3 days later, the cells were lysed with 0.1% triton X-100 and plated for  
691 bacterial burden enumeration using a serial dilution method on plates of Middlebrook 7H11 agar  
692 containing OADC enrichment and BBL MGIT PENTA antibiotics (BD, Cat# 245114). CFUs were  
693 counted after 3 to 4 weeks incubation at 37°C.

694

#### 695 ***Immunofluorescence***

696 For immunofluorescence of GBP1-5, Rab7, and NF- $\kappa$ B, monocyte derived macrophages  
697 (Thp1-macro) were infected with RFP-H37Ra at MOI (multiplicity of infection) 20. The infected  
698 cells were washed twice with pre-warmed PBS four hours and incubated with fresh culture  
699 medium for another 8 hours. Next, the cells were cross-linked with 4% formaldehyde for 15 min  
700 at room temperature and rinsed three times with 1× PBS. The specimen was blocked in blocking  
701 buffer (1× PBS/ 5% normal serum / 0.3% Triton X-100) for 60 min. After blocking, respective  
702 antibodies (GBP1-5, Santa Cruz, sc-166960 AF488; Rab7, Santa Cruz, sc-376362 AF488; NF- $\kappa$ b

703 p65, Santa Cruz, sc-8008) in antibody dilution buffer (1× PBS / 1% BSA / 0.3% Triton X-100) at  
704 2 µg/ml final concentration were incubated with the slides overnight at 4 °C. Slides were washed  
705 three times with PBS and stained with DAPI (Life Technologies) and observed under fluorescence  
706 microscope.

707

708 ***Mouse Models***

709 All wild type C57BL/6 mice used in this study were purchased from Beijing Vital River  
710 Laboratory Animal Technology and all the experiments in this study were approved by the  
711 Scientific Ethic Committee of Huazhong Agricultural University (NO. HZAUMO-2019-019) and  
712 maintained at the Laboratory Animal Centre of Huazhong Agriculture University under specific  
713 pathogen-free (SPF) conditions with 12-hour light/dark cycles. Based on the principles of  
714 laboratory animal welfare and ethics, this study optimized the design of the project and strictly  
715 plans the number of animals required. A total of 28 6-week-old female C57BL/6 mice (20±2g)  
716 were planned. Among them, 4 were used for bone marrow macrophage isolation experiments, and  
717 the remaining 24 were used for Mycobacterium tuberculosis H37Ra infection test and AdoCbl  
718 drug treatment experiment.

719

720 ***Animal experiment***

721 For *M.tb* infection, 6 week old female mice (20±2 g) were infected by intravenous injection  
722 with a dose of  $5\times10^6$  cfu/mL of 200µL *M.tb* H37Ra suspension. All animals were randomly  
723 distributed into 2 groups of 12 each. Then mice were received a gavage feeding of AdoCbl (Sigma,  
724 Cat# C0884) at a daily dose of 0.5 mg/kg·bw and equal volume of sterile PBS used as a negative  
725 control. These mice were given the therapy for 1 day post of *M.tb* infection. Mice were euthanized  
726 after 15 days of drug treatment. Lungs and spleen were taken out for histopathological observation  
727 and CFU analysis. A part of left lung was fixed in 4% paraformaldehyde for a minimum time of  
728 48h, and tissues were paraffin embedded to make section for haematoxylin and eosin (H&E)  
729 staining. Homogenates of lungs and spleen were plated for bacterial burden enumeration using a

730 serial dilution method on plates of Middlebrook 7H11 agar containing OADC enrichment and BBL  
731 MGIT PENTA antibiotics (BD, Cat# 245114) for inhibition of contamination. CFUs were counted  
732 after 3 to 4 weeks incubation at 37 °C.

733

#### 734 ***RNA-Seq analysis***

735 FastQC (version: v0.11.8) was used to assess the quality of RNA-Seq reads, and  
736 Trimmomatic<sup>42</sup> (version: 0.33) was used to filter out the low quality bases and adapter sequences.  
737 Clean reads longer than 36 bp at both ends were kept for further processing. TopHat<sup>43</sup> (version:  
738 v2.1.1) with bowtie2<sup>44</sup> (version: 2.3.5.1) was used to align the paired end RNA-Seq reads to human  
739 reference genome (hg19) with transcriptome annotations from Ensembl<sup>45</sup>. HTSeq<sup>46</sup> (version:  
740 0.11.2) was used to count the mapped reads on the transcripts corresponding to each gene.  
741 DESeq2<sup>47</sup> was used for normalization and differential expression analysis with the read counts on  
742 the genes as inputs.

743

#### 744 ***ATAC-Seq analysis***

745 The reads filtering steps were the same as in “***RNA-Seq analysis***”. Trimmed reads were aligned  
746 to the human genome assembly (hg19) with the Burrows-Wheeler Aligner-MEM<sup>48</sup> (version:  
747 0.7.17-r1188). For each sample, SAMtools<sup>49</sup> (version: 1.7) was used to sort the mapped reads by  
748 position. After marking the duplication reads by Picard toolkit (version: 1.119), uniquely mapped  
749 reads and non-redundant sequences were kept for further analysis by SAMtools with the parameter  
750 F: 1024, q 20. F-Seq<sup>50</sup> (version: 3) was used to call ATAC-Seq peaks as ENCODE ATAC-Seq data  
751 analysis pipeline, and the top 100,000 accessible regions for all samples were kept for further analysis.

752

#### 753 ***ChIP-Seq analysis***

754 The reads filtering steps were the same as “***RNA-Seq analysis***”. Burrows-Wheeler Aligner-  
755 MEM<sup>48</sup> (version: 0.7.17-r1188) was applied to map the reads to the human genome assembly  
756 (hg19). Mapped reads were sorted by position and duplications were discarded by SAMtools<sup>49</sup>

757 (version: 1.7). The reads with the mapping quality higher than 30 were considered as uniquely  
758 mapped reads. Peaks were called by MACS2<sup>51</sup> (version: 2.1.1.20160309). For broad peaks, the  
759 parameters were -B --broad -q 0.05. For narrow peaks, the parameter was -B.

760

#### 761 *Annotation of chromatin states of enhancer and promoter*

762 Promoter regions were defined as the genomic regions 1 kb in front of the transcription start  
763 sites (TSS) of RefSeq genes. Repressed promoters were defined as the promoter regions without  
764 H3K4me3 peaks. Bivalent promoters were defined as the promoter regions enriched with  
765 H3K4me3 and H3K27me3 peaks. Active promoters were defined as the promoter regions enriched  
766 with H3K4me3 peaks but without H3K27me3 peaks.

767 For each cell type, the open non-promoter regions with ATAC-Seq peaks were initially selected  
768 as the candidate regions of enhancers. As previously described<sup>52, 53</sup>, the candidate regions with  
769 H3K4me1 peaks were defined as enhancers. The active mark H3K27ac and inactive mark  
770 H3K27me3 were combined to define the different state of enhancers. An enhancer with  
771 H3K27me3 peaks was defined as poised enhancer. If there were H3K27ac peaks located in  
772 enhancer region, the enhancer was defined as active enhancer. The enhancers with neither  
773 H3H27ac nor H3K27me3 peaks were considered as primed state.

774

#### 775 *In situ DLO Hi-C analysis*

776 As the read1 sequences in the 2×150 bp paired-end reads in the *in situ* DLO Hi-C library  
777 contains all the chromatin interaction pair information, only read1 sequences were retained for  
778 further analysis. Linker filtering was conducted with a Java program, DLO Hi-C Tool<sup>54</sup>. Reads  
779 with mapping scores of greater than 32 were retained for subsequent analysis. Via the linker  
780 sequence, the sequences with interaction pairs information were extracted from the raw reads.

781 To increase the alignment rate, the restriction endonuclease recognition site was complemented  
782 at the end of the sequence. Burrows-Wheeler Aligner-ALN<sup>48</sup> (version: 0.7.17-r1188) was used to  
783 align the interaction sequences to the human reference genome (hg19) with the parameter -n 0.

784 Only the uniquely mapped reads with mapping quality (MAPQ) scores of  $\geq 20$  were retained  
785 and paired for further analysis.

786 The reference genome was divided into fragments according to the restriction enzyme sites, and  
787 the uniquely mapped sequence pairs were aligned to the restriction enzyme fragments. If two ends  
788 from a paired-read were mapped to the same restriction enzyme fragment, the paired-read was  
789 considered a self-ligation product. If two ends from a paired-read were mapped to two adjacent  
790 restriction enzyme fragments, the paired-read was considered a religation product. Both the self-  
791 ligation and religation reads were excluded for further analysis. If multiple sequences had both  
792 ends aligned to the same positions, only one sequence was retained for further analysis, since such  
793 reads probably resulted from PCR amplification.

794 To identify chromatin loops, interaction matrices were converted to .hic files by the pre-  
795 command of Juicer Tools<sup>55</sup> with default resolutions. The HiCCUPS algorithm of Juicer Tools was  
796 used to generate loop lists at resolutions of 5 kb, 10 kb and 25 kb.

797

#### 798 ***Single cell DLO Hi-C data analysis***

799 The processing of the sciDLO Hi-C sequencing data are basically as same as the bulk DLO  
800 Hi-C data processing<sup>54</sup>, with modifications in the PETs extraction step to recognize the barcodes  
801 and an additional step to split the final valid reads according to the barcodes. These two additional  
802 steps were implemented in a new sciDLO Hi-C package.

803 In PETs extraction step, the parameter “--fq1 [R1\_file] --fq2 [R2-file] –linker  
804 GTCGGANNNNNNNGCTAGCNNNNNNNTCCGAC --enzyme T^TA^A” were used. For  
805 cell split step, the default parameters were used: 1, 2, 4 differences of hamming distance were  
806 allowed for the comparison between “read barcode VS library barcode”, “barcode1 VS barcode2  
807 (within same reads)”, “barcode R1 VS barcode R2 (barcode within R1 and R2).”

808 Single cell embedding using the scHiCTools package<sup>23</sup>, all cells matrix was generated with 1  
809 Mb resolution. For cell embedding using the “InnerProduct” to calculate the similarity between all  
810 cells, and using MDS method to mapping all cell’s contact matrix to a 2 dimension vector. Thp-

811 *M.tb* cells are classified into “immune highly activated” and “immune lowly activated” by the  
812 threshold of the mean value of all Thp-*M.tb* cell’s “separation score”, which equal to the mean  
813 distance to the closest 4 Thp1-macro cells in the 2 dimension space.

814 To calculate local DoD from single cell data, the bulk cell DoD calculation pipeline was used  
815 with a few modifications including: 1) merged single cell data as input; 2) the “significant  
816 interaction points” in the first step was replaced by the single cell long-range (>20 kb) contacts; 3)  
817 the mean distance was divided by 5 kb, to scale at the same level as the bulk cell DoD value; 4)  
818 sampling the same number of the contacts in the compared regions of different samples when DoD  
819 comparison between samples was performed.

820

### 821 ***Simulation of chromosome three-dimensional structure of single cells***

822 The chromatin were simulated to generate the chromatin 3D structure using software  
823 “nuc\_dynamic”<sup>56</sup>. For global chromosomes simulation, the software was run with the parameter:  
824 “-s 8.0 4.0 2.0 1.0 0.4 0.2 0.1”. For local region structure simulation, the parameter “-s 0.1 0.05  
825 0.01 0.005” was used. And the results were saved as Protein Data Bank (PDB) file format and  
826 visualized with PyMOL software (version: 2.3.0).

827

### 828 ***Hi-C loop analysis***

829 The Thp1-mono and Thp1-macro contact matrices were randomly downsampled to  
830 351,514,529 intrachromosomal contacts (the same number of intrachromosomal contacts as the  
831 Thp1-*M.tb* matrix). The HiCCUPS algorithm was employed to call loops from the normalized  
832 Thp1-mono and Thp1-macro libraries. To find the differential interaction loops between two  
833 samples, the loops were divided into overlapping and nonoverlapping loops. For differential  
834 analysis of overlapping loops, the surrounding 5×5 window was compared between the two  
835 matrices by Wilcoxon tests, as previously described<sup>57</sup>. Loops with p-values of less than 0.05 were  
836 considered significantly different. For nonoverlapping loops, the fold enrichment values of the  
837 peak over all local neighborhoods were also calculated in the sample without the loop, as

838 previously described<sup>58</sup>. If all calculated fold enrichment values of the pixels in the sample without  
839 the loop were lower than 1.3, the peak in the sample with the loop was considered a differential  
840 peak.

841

842 **TAD boundary calling**

843 TAD boundaries were called at a resolution of 40 kb, as previously described<sup>59</sup>. The interaction  
844 frequencies within 2 Mb downstream and 2 Mb upstream were compared with the default  
845 parameters of DomainCaller. The directionality index (DI) was used to quantify the bias in each  
846 bin. Domains were inferred from hidden Markov model (HMM) state calls.

847 If the distance between two TAD boundaries in two samples was within 80 kb, these TAD  
848 boundaries were considered conserved TAD boundaries in the two samples. If the distance between  
849 two TAD boundaries was greater than 80 kb, the two TADs were considered shifted TADs<sup>60</sup>. If one  
850 TAD in the previous cell state corresponded to multiple smaller TADs in the sample of the  
851 subsequent cell state, the TAD was considered a separated TAD. If multiple small TADs in the  
852 previous cell state corresponded to a large TAD in the subsequent cell state, this TAD was  
853 considered a fused TAD.

854 The hiclib library was applied to distinguish A and B compartments as previously described<sup>61</sup>.  
855 If the values in the first eigenvector were higher than 0, the corresponding bins were marked as A  
856 compartments. If the values in the first eigenvector were smaller than 0, the corresponding bins  
857 were marked as B compartments.

858

859 **TAD "Degree of Disorder" (DoD) and Co-Regulation Score (CRS) calculation**

860 The significant chromatin interactions were first identified based on a Poisson process model.  
861 The expected value was calculated by considering both distance-dependent decay and the local  
862 interaction background, as described in previous studies<sup>58, 62</sup>. The window parameters  $p$  and  $w$   
863 were set to 4 and 7, respectively, according to previous studies<sup>58, 62</sup>. After allocating all significant  
864 interactions in the TAD contact matrix  $M$ , the  $k$  nearest neighbors  $Pk_i$  with  $k=3$  for each

865 significant interaction  $p_i = (x_i, y_i)$ ,  $i \in [1, n]$  were calculated. The mean distance within contact  
866 matrix ( $MD_i$ ) between the significant point  $p_i$  was measured as the mean distance to its k nearest  
867 neighbors, as shown in Supplementary information, Fig. S2f:

$$868 MD_i = \frac{\sum dist(p_i, p_j)}{k}$$

869 where  $dist(p_i, p_j) = \sqrt{(x_j - x_i)^2 + (y_j - y_i)^2}$  is the Euclidean distance in the matrix heatmap  
870 between  $p_i$  and  $p_j$ . The KDTree data structure was used to accelerate the nearest neighbors  
871 searching process<sup>63</sup>. The mean value of all local  $MDs$ ,  $DoD = \sum MD_i / n$ , in a TAD, which  
872 represented the “disorder state” of the chromatin interactions within the TAD was defined as the  
873 TAD DoD.

874 Since the two-sample Kolmogorov-Smirnov (KS) test is sensitive to differences in both the  
875 location and the shape of the distribution, it was used for statistical comparisons between the TAD  
876 DoD values of two biological samples. Here, the D statistic was calculated as follows:

$$877 D_{n,m} = \sup_x |F_{1,n}(x) - F_{2,m}(x)|$$

878 where sup is the supremum function and  $F_{1,n}$  and  $F_{2,m}$  are the cumulative distribution  
879 functions of the  $MD$  of different samples. For balancing the effect of sequencing depth, all  
880 sample’s contact matrices are reconstructed using the same number of valid reads.

881 The consistency of the overall transcriptional change direction (upregulation or  
882 downregulation) of the genes within a TAD during differentiation and activation was defined as  
883 the TAD CRS. The regulation direction score (DS) of a TAD t was defined as follows:

$$884 DS_t = \frac{\sum_{i \in t} \text{sgn}(\log_2(\text{FoldChange}_i))}{N_t}$$

885 where sgn is the sign function. The TAD CRS was defined as the absolute value of the DS:  
886  $CRS_t = \text{abs}(DS_t)$ .

887

#### 888 ***Collection of GWAS-associated risk SNPs***

889 The TB risk SNPs were obtained from all TB-related GWAS studies. We also obtained two

890 extra GWAS results from the GWAS catalog and UK Biobank GWAS data (**Supplementary Table**  
891 **7**). The GWAS catalog, which was developed by the National Human Genome Research Institute  
892 (NHGRI) and European Molecular Biology Laboratory's European Bioinformatics Institute  
893 (EMBL-EBI), contains 3,923 publications and 134,705 SNP-trait associations<sup>64</sup>. Neale Lab  
894 released a large body of summary statistics from GWAS analyses on its website<sup>65</sup>, including data  
895 for 361,194 individuals from the UK Biobank<sup>66</sup> (194,174 females and 167,020 males). All GWAS  
896 results were filtered with a cutoff p-value of  $< 1 \times 10^{-5}$  and minor allele frequency (MAF) of  $> 0.05$   
897 and are listed in (**Supplementary Table 7**). The p-values for meta-analyses were not adjusted  
898 because the raw GWAS data of several previous GWAS analyses were not available.

899

900 ***Integrated analysis of GWAS, eQTL and Hi-C data***

901 Significant eQTLs associated with risk SNPs were obtained from the GTEx portal, which  
902 includes gene expression data for 48 different tissues<sup>67</sup>. The significant genes associated with TB  
903 risk SNPs are listed in **Supplementary Table 7**. Additionally, chromatin interaction loops with  
904 risk SNPs overlapped with significant eQTL gene regions within relevant tissues were selected for  
905 further investigation and are listed in **Supplementary Table 7**. The R package ggbio was  
906 employed to demonstrate the interactions between SNPs and significant gene regions with Hi-C  
907 loops<sup>68</sup>.

908

909 **DATA AND SOFTWARE AVAILABILITY**

910 The accession number for all sequencing data analyzed in this study have been deposited in  
911 the Gene Expression Omnibus (GEO) under accession GSE143984 and GSE159501. GWAS  
912 catalog, <https://www.ebi.ac.uk/gwas>. UK Biobank GWAS result, <http://www.nealelab.is/uk-biobank>. GTEx, <http://www.gtexportal.org>. ENCODE ATAC-Seq data analysis pipeline,  
913 <https://www.encodeproject.org/documents/0eb389f9-d23d-4053-b25b-1e2826ee5a86/@@download/attachment/ATACpipelineV7.pdf>. Picard toolkit,  
914 <http://broadinstitute.github.io/picard/>. The sciDLO Hi-C data analysis pipeline is available at  
915 <http://broadinstitute.github.io/scidlo/>. The sciDLO Hi-C data analysis pipeline is available at  
916

917 https://github.com/GangCaoLab/sciDLO. The script for DoD calculation is available at  
918 https://github.com/GangCaoLab/MDkNN. The ChIP-seq data of NFkB is available at  
919 http://hgdownload.cse.ucsc.edu/goldenPath/hg19/encodeDCC/wgEncodeSydhTfbs/. The ChIP-  
920 seq data of MED1 and BRD4 is available at  
921 https://www.ncbi.nlm.nih.gov/geo/query/acc.cgi?acc=GSE160670.

922

923

924

- 925     **References**
- 926     36. Cusanovich, D.A. et al. Multiplex single-cell profiling of chromatin accessibility by  
927                 combinatorial cellular indexing. *Science* **348**, 910-914 (2015).
- 928     37. Ramani, V. et al. Massively multiplex single-cell Hi-C. *Nature methods* **14**, 263-266 (2017).
- 929     38. Bintu, B. et al. Super-resolution chromatin tracing reveals domains and cooperative  
930                 interactions in single cells. *Science* **362**, eaau1783 (2018).
- 931     39. Beliveau, B.J. et al. OligoMiner provides a rapid, flexible environment for the design of  
932                 genome-scale oligonucleotide in situ hybridization probes. *Proceedings of the National  
933                 Academy of Sciences of the United States of America* **115** (2018).
- 934     40. Jurka, J. et al. Repbase Update, a database of eukaryotic repetitive elements. *Cytogenetic  
935                 and genome research* **110**, 462-467 (2005).
- 936     41. Guan, J., Liu, H., Shi, X., Feng, S. & Huang, B. Tracking multiple genomic elements using  
937                 correlative CRISPR imaging and sequential DNA FISH. *Biophysical journal* **112**, 1077-  
938                 1084 (2017).
- 939     42. Bolger, A.M., Lohse, M. & Usadel, B. Trimmomatic: a flexible trimmer for Illumina  
940                 sequence data. *Bioinformatics* **30**, 2114-2120 (2014).
- 941     43. Trapnell, C., Pachter, L. & Salzberg, S.L. TopHat: discovering splice junctions with RNA-  
942                 Seq. *Bioinformatics* **25**, 1105-1111 (2009).
- 943     44. Langmead, B. & Salzberg, S.L. Fast gapped-read alignment with Bowtie 2. *Nature methods*  
944                 **9**, 357 (2012).

- 945 45. Clamp, M. et al. Ensembl 2002: accommodating comparative genomics. *Nucleic Acids*  
946 *Research* **31**, 38-42 (2003).
- 947 46. Anders, S., Pyl, P.T. & Huber, W. HTSeq—a Python framework to work with high-  
948 throughput sequencing data. *Bioinformatics* **31**, 166-169 (2015).
- 949 47. Love, M.I., Huber, W. & Anders, S. Moderated estimation of fold change and dispersion  
950 for RNA-seq data with DESeq2. *Genome biology* **15**, 550 (2014).
- 951 48. Li, H. & Durbin, R. Fast and accurate long-read alignment with Burrows-Wheeler  
952 transform. *Bioinformatics* **26**, 589-595 (2010).
- 953 49. Li, H. et al. The sequence alignment/map format and SAMtools. *Bioinformatics* **25**, 2078-  
954 2079 (2009).
- 955 50. Boyle, A.P., Guinney JCrawford, G.E. & Furey, T.S. F-Seq: a feature density estimator for  
956 high-throughput sequence tags. *Bioinformatics* **24**, 2537-2538 (2008).
- 957 51. Zhang, Y. et al. Model-based Analysis of ChIP-Seq (MACS). *Genome biology* **9**, R137  
958 (2008).
- 959 52. Chen, H. et al. A pan-cancer analysis of enhancer expression in nearly 9000 patient samples.  
960 *Cell* **173**, 386–399.e312 (2018).
- 961 53. Minoux, M. et al. Gene bivalency at polycomb domains regulates cranial neural crest  
962 positional identity. *Science* **355**, eaal2913 (2017).
- 963 54. Hong, P. et al. The DLO Hi-C Tool for Digestion-Ligation-Only Hi-C Chromosome  
964 Conformation Capture Data Analysis. *Genes* **11**, 289 (2020).

- 965 55. Durand, N.C. et al. Juicer provides a one-click system for analyzing loop-resolution Hi-C  
966 experiments. *Cell Syst.* **3**, 95–98 (2016).
- 967 56. Stevens, T.J. et al. 3D structures of individual mammalian genomes studied by single-cell  
968 Hi-C. *Nature* **544**, 59-64 (2017).
- 969 57. Kim, Y.H. et al. Rev-erba dynamically modulates chromatin looping to control circadian  
970 gene transcription. *Science* **359**, 1274–1277 (2018).
- 971 58. Rao, S.S. et al. A 3D map of the human genome at kilobase resolution reveals principles of  
972 chromatin looping. *Cell* **159**, 1665–1680 (2014).
- 973 59. Dixon, J.R. et al. Topological domains in mammalian genomes identified by analysis of  
974 chromatin interactions. *Nature* **485**, 376-380 (2012).
- 975 60. Zirkel, A. et al. HMGB2 loss upon senescence entry disrupts genomic organization and  
976 induces CTCF clustering across cell types. *Mol. Cell* **70**, 730–744.e736 (2018).
- 977 61. Maxim, I. et al. Iterative correction of Hi-C data reveals hallmarks of chromosome  
978 organization. *Nat. Methods* **9**, 999–1003 (2012).
- 979 62. Wang, X.-T., Dong, P.-F., Zhang, H.-Y. & Peng, C. Structural heterogeneity and functional  
980 diversity of topologically associating domains in mammalian genomes. *Nucleic Acids Res.*  
981 **43**, 7237–7246 (2015).
- 982 63. Bentley, J.L. Multidimensional binary search trees used for associative searching. *Commun.*  
983 *ACM* **18**, 509–517 (1975).
- 984 64. MacArthur, J. et al. The new NHGRI-EBI catalog of published genome-wide association

- 985 studies (GWAS catalog). *Nucleic Acids Res.* **45**, D896–D901 (2016).
- 986 65. Bycroft, C. et al. The UK Biobank resource with deep phenotyping and genomic data.  
987 *Nature* **562**, 203–209 (2018).
- 988 66. Sudlow, C. et al. UK Biobank: an open access resource for identifying the causes of a wide  
989 range of complex diseases of middle and old age. *PLoS Med.* **12**, e1001779 (2015).
- 990 67. Lonsdale, J. et al. The genotype-tissue expression (GTEx) project. *Nat. Genet.* **45**, 580–  
991 585 (2013).
- 992 68. Yin, T., Cook, D. & Lawrence, M. ggbio: an R package for extending the grammar of  
993 graphics for genomic data. *Genome Biol.* **13**, R77 (2012).
- 994

995    **Acknowledgements**

996    This work was supported by the National Key Research and Development Project of China  
997    (grant 2017YFD0500300 and 2016YFA0102500 to G.C.), the National Natural Science  
998    Foundation of China (grants 31970590 and 31771402 to G.L., 31872470 to G.C., and 31900432  
999    to D.L.), Fundamental Research Funds for the Central Universities (grants 2662017PY116 to  
1000    G.L., and 2662018PY025 and 2662019YJ004, to G.C.), National Postdoctoral Program for  
1001    Innovative Talents (grant BX20180113, to D.L.), China Postdoctoral Science Foundation (grant  
1002    2018M640710, to D.L.)

1003

1004    **Author contributions**

1005    G.C., G.L., and D.L. contributed with conception of the project and experiment design. D.L., Z.Z.,  
1006    S.Z., L.X., Q.X., J.W., Y.H., X.W., C.C., and Z.C conducted the *in situ* DLO Hi-C, sciDLO Hi-C,  
1007    ChIP-Seq, ATAC-Seq, RNA-seq, Immunofluorescence, DNA-FISH experiments and generated  
1008    data. D.L., B.Y., W.Z., Z.H., and R.Y. conducted CRISPR knocked out experiments. W.X., P.H.,  
1009    C.W., C.W., J.M., and X.H. performed data analysis and interpretation. D.L., G.C., G.L., W.X.,  
1010    P.H., and C.W. wrote the manuscript, with input from all other authors. Z.F. revised the manuscript.  
1011    G.C., and G.L. supervise the project.

1012

1013    **Conflict of Interest**

1014    The authors declare no competing interests.

1015

1016

1017

1018

1019

1020

1021 **Figure and table legends**

1022 **Fig. 1 | Decoding the 3D Genome of monocytes, macrophages, and *M.tb* infected macrophages**  
1023 **with single cell indexed (sci) DLO Hi-C.** **a**, Representative calcein and hoechst fluorescence  
1024 staining images of Thp1-mono, Thp1-macro, and Thp1-*M.tb* cells. **b**, Flowchart of the sciDLO Hi-  
1025 C method. **c**, Present cluster analysis result of sciDLO Hi-C data sets by using two-dimensional  
1026 scatter plots. **d**, Comparison of average contacts around immune genes ( $\pm 10$  Kb around TSS sites)  
1027 between Thp1-mono, Thp1-macro, and Thp1-*M.tb* cells. **e**, Simulation of chromatin three-  
1028 dimensional conformation of representative immune highly activated and moderately activated  
1029 cells. **f**, Comparison of the spatial location of NOD2 and BRD7 in immune highly activated and  
1030 moderately activated cells by using simulated nucleus. NOD2 and BRD were marked with arrows.

1031  
1032 **Fig. 2 | Evaluating the order and stochasticity of single cell chromatin folding with degree of**  
1033 **disorder (DoD).** **a,b**, Bulk cell chromatin contact matrix and gene expression level of *STAT1* TAD  
1034 of Thp1-macro and Thp1-*M.tb* cells. The chromatin interaction hot spot which formed in low DOD  
1035 TAD were marked by dashed box. Chromatin loop mediated *STAT1* and enhancer interaction were  
1036 labeled by arrows. **c,d**, Single cell chromatin contacts around *STAT1* gene of Thp1-macro and  
1037 Thp1-*M.tb* cells. Individual cells have similar chromatin folding patterns in the low DoD TAD. **e**,  
1038 Illustration of the TAD degree of disorder (DoD) which was used to measure the order and  
1039 consistency of chromatin folding in single cells. **f**, DoD values of Thp1-mono and Thp1-macro  
1040 around MYC gene region by using bulk cell DLO Hi-C data sets. **g**, Relationship between TAD  
1041 DoD and average gene expression level (normalized read count) in Thp1-mono, Thp1-macro, and  
1042 Thp1-*M.tb*, respectively. The DoD value higher than median was defined as “High DoD”; lower  
1043 than the median was defined as “Low DoD”. Significance of differences was measured by  
1044 Kolmogorov-Smirnov test. **h**, Correlation between the TAD DoD and A, B compartments. In x  
1045 axis, B/A means the TADs which contains both A and B compartments. Significance of differences  
1046 was measured by unpaired one-sided t test. **i**, Correlation between the TAD DoD and coregulation  
1047 score (CRS). TADs with lower TAD DoD preferentially have higher CRS, underlying more

1048 coordinated gene regulation in such TADs. x axis is the average value of the quantile groups with  
1049 the lowest, low, high and highest TAD DoDs, respectively. **j**, Absolute values of the log2 fold  
1050 changes in gene expression (y-axis) in the boundary not changed but DoD value significant  
1051 changed TADs (dynamic DoD), boundary and DoD unchanged TADs (static DoD), boundary  
1052 shifted TADs (shifted), boundary fused TADs (fused), and boundary divided TADs (divided)  
1053 during differentiation and infection.

1054

1055 **Fig. 3 | Low DoD is associated with active epigenetic modification and high gene expression**  
1056 **level. a,b,** Correlation between TAD DoD and chromatin epigenetic profile. The y axis shows the  
1057 normalized ChIP-seq peaks per TAD. The DoD value higher than median was defined as “High  
1058 DoD”; lower than the median was defined as “Low DoD”. Significant differences were measured  
1059 by unpaired one-sided t test. **c,** Correlation between TAD DoD and chromatin accessibility. Each  
1060 dot represents one TAD. x-axis is the number of ATAC peaks per Mb. **d,e,** Chromatin contact  
1061 matrix and DoD value changes around HERC5 and HERC6 gene region after *M.tb* infection. **f,g,**  
1062 RNA expression level, chromatin accessibility, H3K27ac, and H3K4me4 histone modification  
1063 changes after *M.tb* infection. **h,i,** Simulated three-dimensional structure of HERC5 and HERC6  
1064 gene region during *M.tb* infection by using bulk cell DLO Hi-C data sets. **j,** The relationship  
1065 between DoD value, chromatin folding order, chromatin accessibility, gene transcription  
1066 coregulation, and histone modification.

1067

1068 **Fig. 4 | Remodeling of the chromatin configuration of guanylate-binding protein (GBP) gene**  
1069 **clusters. a,** Comparison of TAD DoD value, chromatin interaction matrices, chromatin loops,  
1070 RNA expression levels and epigenetic modifications around the GBP loci in bulk cells before and  
1071 after *M.tb* infection. **b,** Comparing the single cell chromatin contact differences using merged  
1072 single cell chromatin contact matrix. Each color of the dots in the matrix represents the chromatin  
1073 contact from the same cell. **c,** Single cell chromatin contacts between *GBP2*, *GBP4*, *GBP5*, and  
1074 *GBP7* and RNA expression before and after *M.tb* infection. **d,** Depiction Hi-C chromatin loops

1075 before and after infection and BRD4 and MED1 ChIP-seq peaks around *GBP* gene clusters. **e**, Co-  
1076 localization between BRD4 and the *GBP* gene cluster by IF and DNA-FISH in Thp1-macro and  
1077 Thp1-*M.tb* cells. IF, DNA-FISH, and merged channels (overlapping signal in white) are shown in  
1078 separate images. The dashed line highlights the nuclear periphery, determined by DAPI staining.  
1079 The rightmost column shows the area in the yellow box in greater detail. Each cell type, we counted  
1080 60 *GBP* gene loci, 18.3% (11/60) *GBP* loci were co-located with BRD4 in Thp1-macro cells and  
1081 65.0% (39/60) *GBP* loci were co-located with BRD4 in Thp1-*M.tb* cells.

1082

1083 **Fig. 5 | Reorganization of chromatin architecture around NF-κB target gene sites.** **a**, Overall  
1084 TAD DoD of THP-1 cells during differentiation and infection. The y-axis represents the average  
1085 DoD value of TADs in each state. **b**, The relationship between TAD DoD and chromatin loop  
1086 during differentiation and activation. The x-axis represents log2 fold change of TAD DoD value,  
1087 and the y-axis represent the number of loop changes in each TAD. **c**, Compare NF-κB enrichment  
1088 around transcription start site ( $\pm 3$  Kb) between strengthened loop anchor gene and random control  
1089 gene. The gene in the heatmap were sorted according to the enrichment intensity of NF-κB. ChIP-  
1090 seq data is from ENCODE (GM12891 cell line). **d**, Immunofluorescence analysis of NF-κB (p65)  
1091 subcellular location before and after *M.tb* infection. **e**, Log2 fold changes of ATAC peaks and RNA  
1092 expression level of NF-κB target genes (n=435) and random control genes. Significant differences  
1093 were calculated by unpaired one-sided t test. **f**, The ratio of strengthened loop/total loop of NF-κB  
1094 target gene sites and random control sites. **g**, Chromatin loop remodeling and TAD DoD changes  
1095 in typical NF-κB target gene loci. **h**, Bulk cell and merged single cell chromatin interaction  
1096 matrices around IFIT gene locus. Cells with more consistent chromatin interaction were marked  
1097 with a dashed line. **i,j**, Comparison of chromatin loop configurations, RNA expression levels, and  
1098 epigenetic modifications of the IFIT gene family locus before (**i**) and after (**j**) *M.tb* infection. The  
1099 arrows in (**j**) indicate the potential cis element linked with IFIT2, IFIT3, and IFIT1. **k**, Schematic  
1100 diagram of chromatin remodeling of NF-κB target genes during infection.

1101

1102 **Fig. 6 | Functional identification of PD-L1 enhancer.** **a**, Interaction of the PD-L1 enhancer and  
1103 promoter in the Hi-C matrix. **b,c**, Genome Browser view of RNA expression levels, chromatin  
1104 accessibility, and histone modifications at the PD-L1 gene and enhancer regions in Thp1-macro  
1105 and Thp1-*M.tb* cells. NF-κB ChIP-seq peaks (ENCODE, GM15510 cell line) and strengthened  
1106 ATAC-seq peaks were marked by arrows. **d**, ChIP-qPCR validation of the NF-κB (P65) enrichment  
1107 on the PD-L1 enhancer and promoter regions. The amount of immunoprecipitated DNA in each  
1108 sample is represented as signal relative to the total amount of input chromatin (y-axis). Significant  
1109 differences were calculated by unpaired one-sided t test. **e**, Experimental design of sgRNA-guided  
1110 enhancer perturbation by the Cas9 protein. **f**, Relative mRNA expression levels of *PD-L1* in Thp1-  
1111 macro cells and the same line after enhancer deletion. Error bars show mean ± SE of results of  
1112 three replicates; the difference was assessed using unpaired one-sided t test. **g**, PD-L1 protein  
1113 levels in Thp1-macro cells and the same cell line after enhancer deletion before and after *M.tb*  
1114 infection. **h**, Schematic of enhancer-promoter interaction mediated regulation of PD-L1 expression  
1115 during *M.tb* infection.

1116

1117 **Fig. 7 | Identification of long range regulatory target genes of TB susceptibility loci and novel**  
1118 **anti-TB drug targets by integrated multi-omics analysis.** **a**, Identification of long range  
1119 regulatory target genes of TB susceptibility loci, LRRK2 by integrated eQTL, Hi-C and GWAS  
1120 multi-omics analysis. **b**, The rs1873613 SNP is located in the anchor of the LRRK2 gene chromatin  
1121 loop, which is significantly strengthened after *M.tb* infection, as shown in the Hi-C matrix. **c**,  
1122 Simulated typical single cell chromatin structure of SNP rs1873613 and LRRK2 gene region  
1123 before and after *M.tb* infection. **d**, Regulation of LRRK2 gene expression by the rs1873613 SNP.  
1124 The x axis indicates three genotypes of individuals from the Genotype-Tissue Expression (GTEx)  
1125 dataset. **e,f**, Immunofluorescence analysis and quantification of the co-localization of the *M.tb*  
1126 (H37Ra-RFP) and Rab7 in bone marrow-derived macrophages treated with the LRRK2 inhibitor  
1127 AdoCbl and PBS (control). **g**, CFU assays of *M.tb* in bone-marrow-derived macrophage cells  
1128 treated with AdoCbl and PBS (control). Significant differences were calculated by unpaired one-

1129 sided t test. **h,i**, CFU assays of *M.tb* in C57BL/6 mouse lungs treated with AdoCbl and PBS  
1130 (control). Significant differences were calculated by unpaired one-sided t test. **j**, HE-stained lung  
1131 and spleen sections in the AdoCbl and control (PBS) groups. Obvious lesions in the lungs and  
1132 spleen are highlighted by the dashed lines.

1133

1134 **Extended Data Fig. 1 | Transcription dynamics and three-dimensional genome structure of**  
1135 **single cell of THP-1 cells.** **a**, Clustering of gene expression profiles in THP-1 cells during  
1136 differentiation and *M.tb* infection. The heatmap shows the relative expression levels of genes (rows)  
1137 in each sample (column). **b**, MA plot for gene differential expression analysis during THP-1 cell  
1138 differentiation. Important transcription factors related to cell proliferation and differentiation are  
1139 highlighted. **c**, MA plot for gene differential expression analysis during *M.tb* infection. Marker  
1140 genes and important transcription factors for macrophages and M1 macrophages are highlighted.  
1141 **d**, Recovery of 80 bp proximity ligation junction DNA by DNA PAGE gel during sciDLO Hi-C.  
1142 **e**, Junction reads between different single cell Hi-C data sets. **f**, The structures of sequence adapter,  
1143 80bp junction contact DNA and amplification primers used in sciDLO Hi-C experiment. **g**,  
1144 Simulated single cell 3D genome structure of Thp1-mono, Thp1-macro, and Thp1-*M.tb* cells at 25  
1145 kb resolution. **h**, Identifying chromatin territories by using simulated single cell nucleus. **i**, Pearson  
1146 coefficient of merged single cell chromosome 1 contact matrix and bulk cell chromosome 1 contact  
1147 matrix.

1148

1149 **Extended Data Fig. 2 | Calculation of TAD degree of disorder (DoD) in three types of cells.** **a**,  
1150 Histone modification, DNase clusters, and transcription factor enrichment in the STAT1 enhancer  
1151 region. The transcription factors regulating the PD-L1 gene are marked by arrows. Data are from  
1152 the UCSC Genome browser (<http://genome.ucsc.edu>). **b**, Illustration of computational pipeline for  
1153 determining the TAD DoD. First, the local expectation of chromatin interactions was estimated  
1154 using the distance decay function and donut filter. Then, the p-value of each point in the contact  
1155 matrix was calculated and screened using a Poisson process model. The average distance to each

1156 significant point's k-nearest neighbors was designated as the MD (mean distance). The TAD DoD  
1157 was calculated as the average value of the MD of all points. **c**, Histogram showing the MD  
1158 distribution before and after *M.tb* infection in the GBP region (Chr1:89,360,000-89,920,000). **d**,  
1159 The cumulative histogram used in the KS (Kolmogorov-Smirnov) test for statistical comparison  
1160 of the MD distribution in (**c**); here, the D statistic was equal to 0.261, and the p-value was equal to  
1161 3.852e-8. **e**, Examples of TADs with different TAD DoDs. From left to right, the TAD DoD value  
1162 is increasing. **f**, The TAD DoD distribution in all three cell types. The x-axis represents the TAD  
1163 DoD value and the y-axis represents the kernel density estimation (KDE) value. **g**, Schematic  
1164 illustrating the calculation of gene coregulation score (CRS) in TAD. **h**, TAD dynamics of THP-1  
1165 cells during differentiation and activation. **i**, DoD dynamics of boundary intact TADs during  
1166 differentiation and infection.

1167

1168 **Extended Data Fig. 3 | Chromatin state dynamics of THP-1 cells during differentiation and**  
1169 ***M.tb* infection.** **a**, Chromatin state definitions and histone mark probabilities. Average genome  
1170 coverage, genomic annotation enrichment levels, and gene expression levels in each chromatin  
1171 state of Thp1-mono, Thp1-macro, and Thp1-*M.tb* cells, respectively. The difference in the  
1172 chromatin state in each sample is highlighted with an arrow. **b**, Definition of enhancer and  
1173 promoter states. **c**, Dynamics of enhancer and promoter states during THP-1 cell differentiation  
1174 and *M.tb* infection. **d**, Relationship between gene expression levels and histone modifications in  
1175 promoter regions. Scatterplots correlating H3K27me3 (x axis), H3K4me3, H3K27ac, and  
1176 H3K9me3 (y axis) enrichment levels (log2) at the promoter regions (transcription start site (TSS)  
1177  $\pm$  1 kb) in Thp1-mono, Thp1-macro, and Thp1-*M.tb* cells, respectively. The color codes indicate  
1178 RNA log<sub>2</sub> fold changes. **e**, KEGG pathway analysis of the 423 genes whose promoter status  
1179 changed from repressive to active after *M.tb* infection.

1180

1181 **Extended Data Fig. 4 | Verify the co-location of GBP gene cluster and MED1 protein.** **a**,  
1182 Immunofluorescence analysis of GBP protein distribution around *M.tb* in THP-1 macrophages. **b**,

1183 Co-localization between MED1 and the *GBP* gene cluster by IF and DNA-FISH in Thp1-macro  
1184 and Thp1-*M.tb* cells. IF, DNA-FISH, and merged channels (overlapping signal in white) are shown  
1185 in separate images. The dashed line highlights the nuclear periphery, determined by DAPI staining.  
1186 The rightmost column shows the area in the yellow box in greater detail. Each cell type, we counted  
1187 60 *GBP* loci, 15.0 % (9/60) *GBP* loci were co-located with MED1 in Thp1-macro cells and 51.6 %  
1188 (31/60) *GBP* loci were co-located with MED1 in Thp1-*M.tb* cells.

1189

1190 **Extended Data Fig. 5 | Transcription factor NF-κB is involved in the strengthening of target**  
1191 **chromatin loops during *M.tb* infection.** **a**, log2 fold changes of overall TAD DoD value of THP-  
1192 1 cells during differentiation and infection. **b**, Log2 RNA expression fold changes of the immune  
1193 genes which located in the strengthened (immune gene, n= 229) and weakened (immune gene,  
1194 n=112) loop anchors. Significant differences were calculated by unpaired one-sided t test. **c**,  
1195 Dynamic immune gene-regulatory element chromatin interaction network during *M.tb* infection.  
1196 **d**, KEGG pathway enrichment analysis of the genes located in strengthened loop anchors. **e**, ChIP-  
1197 qPCR validation of the NF-κB (P65) enrichment on the loop anchor of the NF-κB target genes.  
1198 The amount of immunoprecipitated DNA in each sample is represented as signal relative to the  
1199 total amount of input chromatin (y-axis). Significant differences were calculated by unpaired one-  
1200 sided t test.

1201

1202 **Extended Data Fig. 6 | PD-L1 enhancer identification and knockout.** **a,b**, Histone modification  
1203 and transcription factor enrichment in the PD-L1 promoter and enhancer region. The transcription  
1204 factors regulating the PD-L1 gene are marked by arrows. Data are from the UCSC Genome  
1205 browser (<http://genome.ucsc.edu>). **c**, sgRNAs used in PD-L1 enhancer deletion. Two sgRNAs  
1206 were designed for each side of the PD-L1 enhancer. **d,e**, Validation of homozygous PD-L1  
1207 enhancer deletion. **f**, Genotype of wild-type and PD-L1 enhancer-deleted THP-1 cells as  
1208 determined by PCR.

1209

1210 **Extended Data Fig. 7 | Comprehensive map of potential tuberculosis susceptibility genes by**  
1211 **integrated eQTL, Hi-C and GWAS multi-omics analysis.** **a**, Circos plot of all reported TB risk  
1212 SNPs and significant eQTLs associated with risk SNPs, with the corresponding gene expression  
1213 levels, histone modifications and Hi-C loops on chromosome 12. **b**, Identification of target genes  
1214 of TB susceptibility SNPs by integrated eQTL, Hi-C and GWAS multi-omics analysis. **c,d**,  
1215 Comparison of the dynamic chromatin loops around the potential targets NSL1 (**c**) and ASAP1 (**d**)  
1216 before and after *M.tb* infection. The strengthened loops and TB susceptibility SNPs are highlighted  
1217 by arrow. **e**, Binding of transcription factors around SNP rs1873613. Data are adapted from the  
1218 UCSC browser (<http://genome.ucsc.edu>). **f**, The mechanism by which the rs1873613 SNP causes  
1219 TB susceptibility and the role of AdoCbl in the treatment of TB.

1220

1221 **Supplementary Table 1.** Differentially expressed genes during THP-1 cell differentiation.

1222

1223 **Supplementary Table 2.** Differentially expressed genes during *M.tb* infection.

1224

1225 **Supplementary Table 3.** Key performance metrics of merged sciDLO Hi-C library. In order to  
1226 distinguish between single cells, we added two rounds of barcodes. In the first round, we added 96  
1227 barcodes to the 96-well plate, and in the second round, we added 14 barcodes in the sequencing  
1228 adapter.

1229

1230 **Supplementary Table 4.** Key performance metrics of different *in situ* DLO Hi-C library, including  
1231 uniquely mapped reads (for mapping efficiency evaluation), non-redundantly mapped reads (for  
1232 PCR redundancy evaluation), intra- or inter-chromosomal contact (for random ligation noise  
1233 evaluation), and intra-short- or intra-long-range contact (for the noise of the dangling end and self-  
1234 ligation reads evaluation).

1235

1236 **Supplementary Table 5.** Dynamics of promoter and enhancer states during THP-1 cell

1237 differentiation and *M.tb* infection.

1238

1239 **Supplementary Table 6.** Loop anchor-located genes associated with chromatin remodeling during  
1240 *M.tb* infection.

1241

1242 **Supplementary Table 7.** Integrated GWAS summary and eQTL information.

1243

1244 **Supplementary Table 8.** Barcoded linker, MGI-2000 platform sequence adapter, and barcoded  
1245 amplification primer used in sciDLO Hi-C library construction.

1246

1247

1248

1249

# Figures

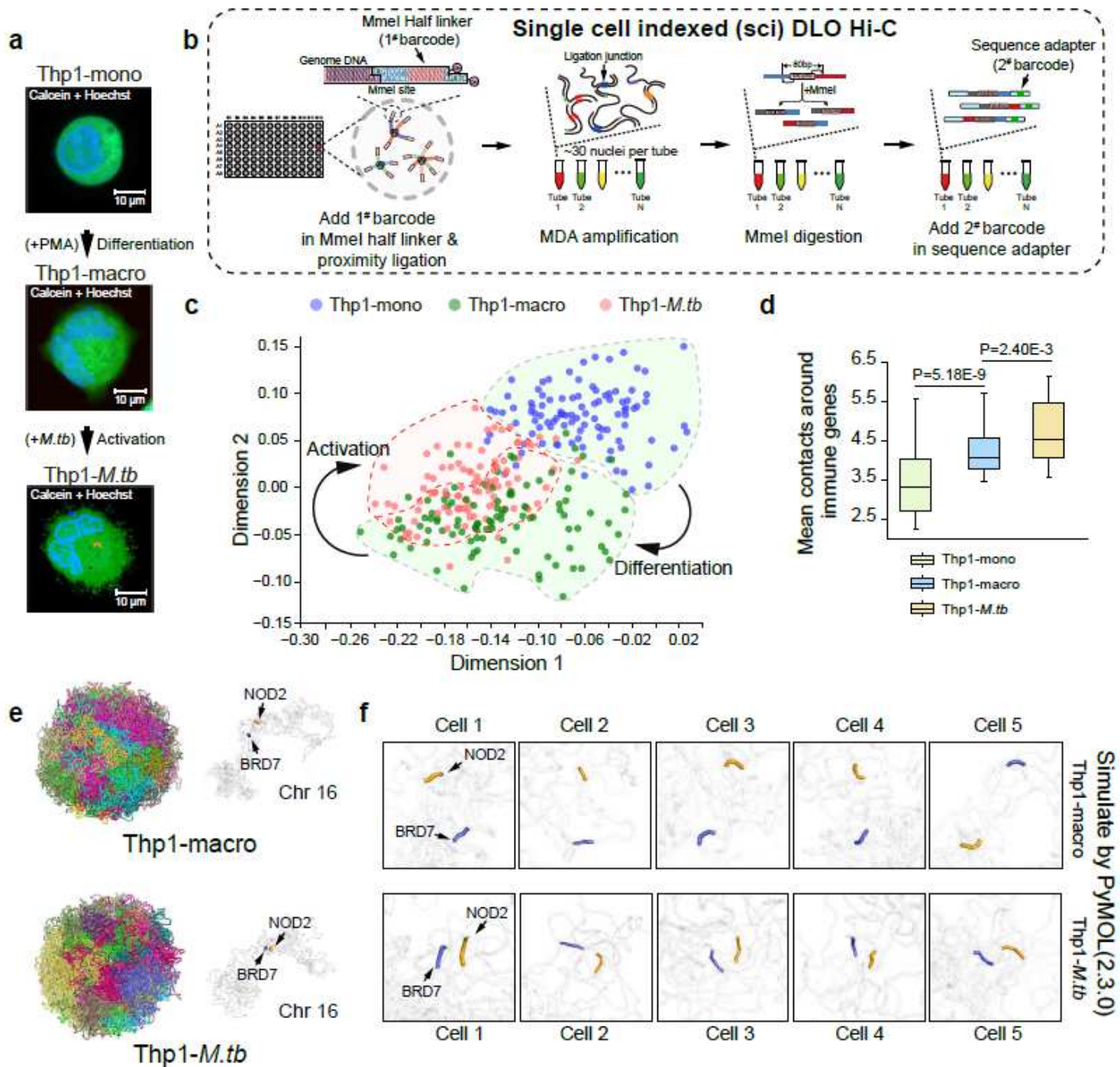


**Figure 1**

Decoding the 3D Genome of monocytes, macrophages, and M.tb infected macrophages with single cell indexed (sci) DLO Hi-C. a, Representative calcein and hoechst fluorescence staining images of Thp1-mono, Thp1-macro, and Thp1-M.tb cells. b, Flowchart of the sciDLO Hi-C method. c, Present cluster analysis result of sciDLO Hi-C data sets by using two-dimensional scatter plots. d, Comparison of average contacts around immune genes ( $\pm 10$  Kb around TSS sites) between Thp1-mono, Thp1-macro, and Thp1-M.tb cells. e, Simulation of chromatin three-dimensional conformation of representative immune highly

activated and moderately activated cells. f, Comparison of the spatial location of NOD2 and BRD7 in immune highly activated and moderately activated cells by using simulated nucleus. NOD2 and BRD were marked with arrows.

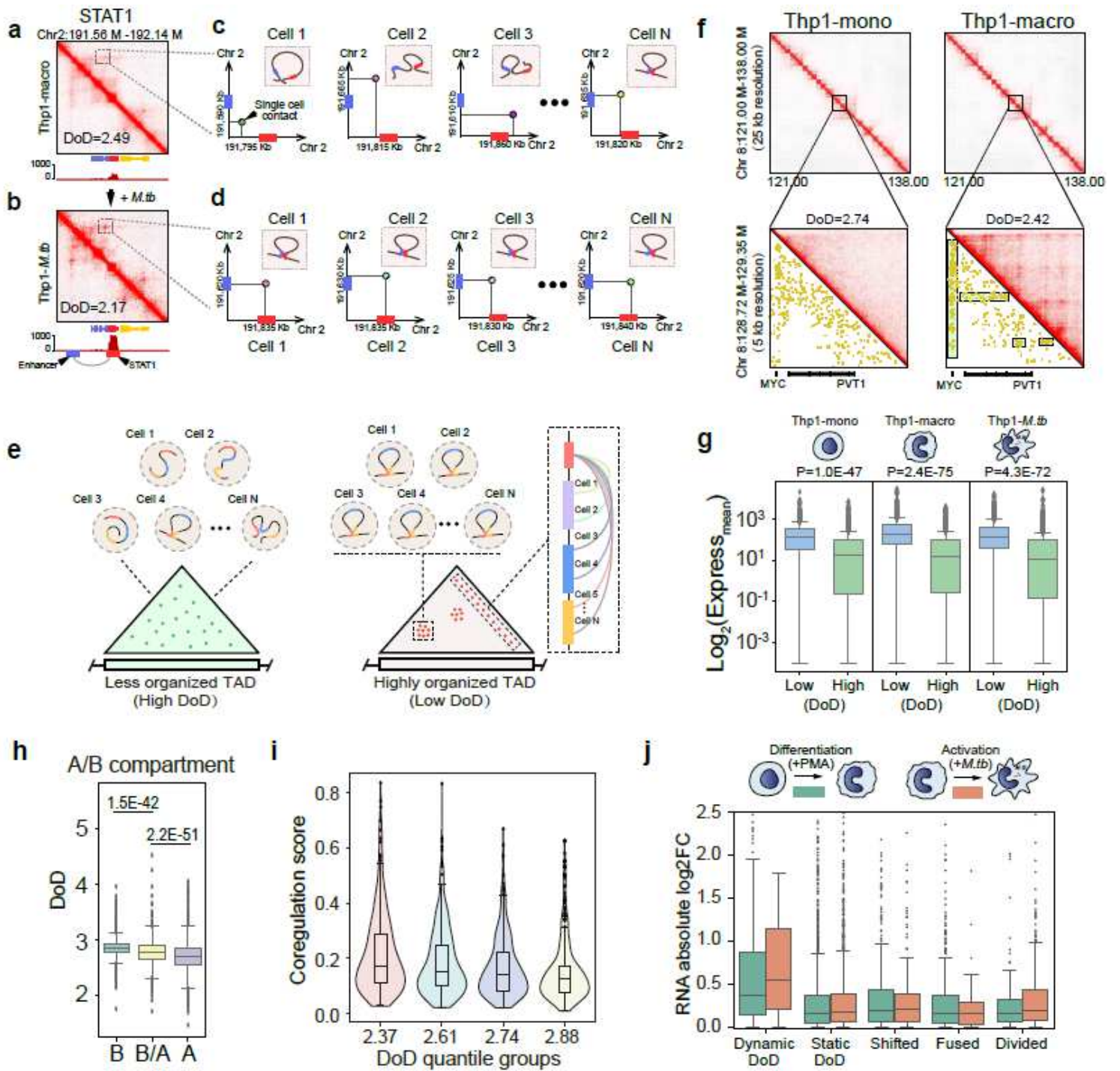


**Figure 2**

Evaluating the order and stochasticity of single cell chromatin folding with degree of disorder (DoD). a,b, Bulk cell chromatin contact matrix and gene expression level of STAT1 TAD of Thp1-macro and Thp1-M.tb cells. The chromatin interaction hot spot which formed in low DOD TAD were marked by dashed box. Chromatin loop mediated STAT1 and enhancer interaction were labeled by arrows. c,d, Single cell

chromatin contacts around STAT1 gene of Thp1-macro and Thp1-M.tb cells. Individual cells have similar chromatin folding patterns in the low DoD TAD. e, Illustration of the TAD degree of disorder (DoD) which was used to measure the order and consistency of chromatin folding in single cells. f, DoD values of Thp1-mono and Thp1-macro around MYC gene region by using bulk cell DLO Hi-C data sets. g, Relationship between TAD DoD and average gene expression level (normalized read count) in Thp1-mono, Thp1-macro, and Thp1-M.tb, respectively. The DoD value higher than median was defined as "High DoD"; lower than the median was defined as "Low DoD". Significance of differences was measured by Kolmogorov-Smirnov test. h, Correlation between the TAD DoD and A, B compartments. In x axis, B/A means the TADs which contains both A and B compartments. Significance of differences was measured by unpaired one-sided t test. i, Correlation between the TAD DoD and coregulation score (CRS). TADs with lower TAD DoD preferentially have higher CRS, underlying more coordinated gene regulation in such TADs. x axis is the average value of the quantile groups with the lowest, low, high and highest TAD DoDs, respectively. j, Absolute values of the log<sub>2</sub> fold changes in gene expression (y-axis) in the boundary not changed but DoD value significant changed TADs (dynamic DoD), boundary and DoD unchanged TADs (static DoD), boundary shifted TADs (shifted), boundary fused TADs (fused), and boundary divided TADs (divided) during differentiation and infection.

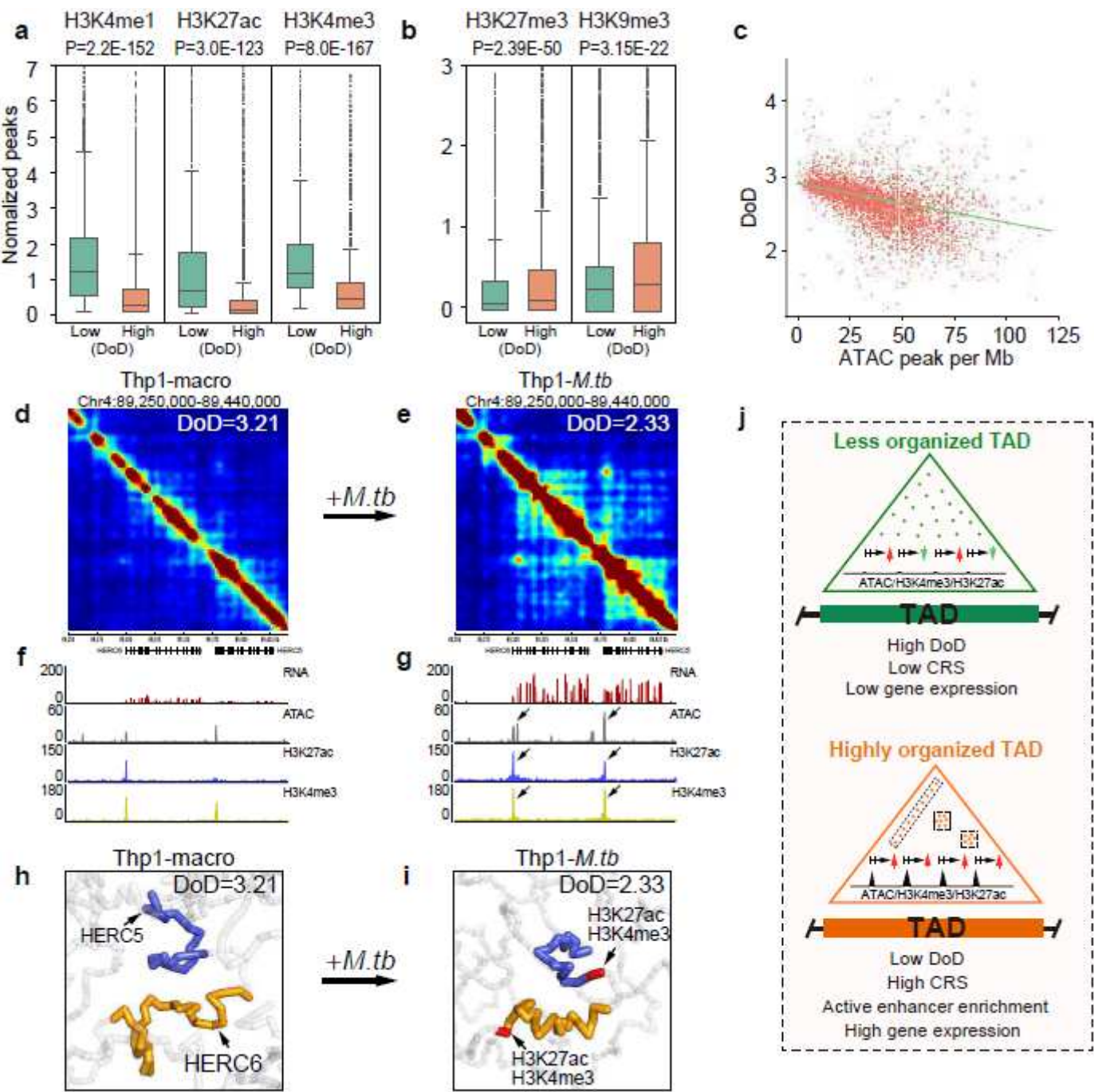


**Figure 3**

Low DoD is associated with active epigenetic modification and high gene expression level. **a,b**, Correlation between TAD DoD and chromatin epigenetic profile. The y axis shows the normalized ChIP-seq peaks per TAD. The DoD value higher than median was defined as “High DoD”; lower than the median was defined as “Low DoD”. Significant differences were measured by unpaired one-sided t test. **c**, Correlation between TAD DoD and chromatin accessibility. Each dot represents one TAD. x-axis is the number of ATAC peaks per Mb. **d,e**, Chromatin contact matrix and DoD value changes around HERC5 and HERC6 gene region after *M.tb* infection. **f,g**, RNA expression level, chromatin accessibility, H3K27ac, and H3K4me4 histone modification changes after *M.tb* infection. **h,i**, Simulated three-dimensional structure of

HERC5 and HERC6 gene region during M.tb infection by using bulk cell DLO Hi-C data sets. j, The relationship between DoD value, chromatin folding order, chromatin accessibility, gene transcription coregulation, and histone modification.

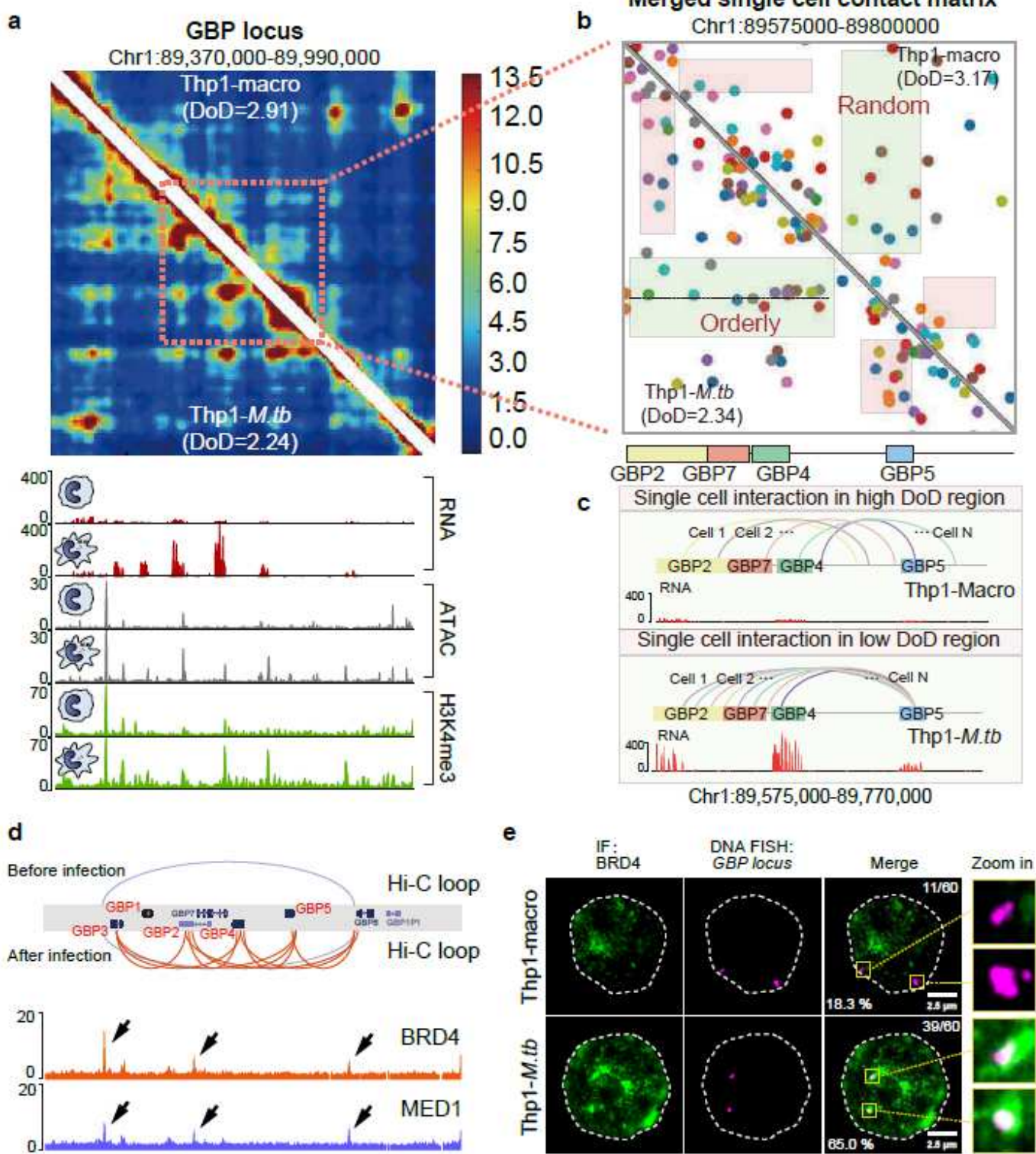


**Figure 4**

Remodeling of the chromatin configuration of guanylate-binding protein (GBP) gene clusters. a, Comparison of TAD DoD value, chromatin interaction matrices, chromatin loops, RNA expression levels

and epigenetic modifications around the GBP loci in bulk cells before and after M.tb infection. b, Comparing the single cell chromatin contact differences using merged single cell chromatin contact matrix. Each color of the dots in the matrix represents the chromatin contact from the same cell. c, Single cell chromatin contacts between GBP2, GBP4, GBP5, and GBP7 and RNA expression before and after M.tb infection. d, Depiction Hi-C chromatin loops before and after infection and BRD4 and MED1 ChIP-seq peaks around GBP gene clusters. e, Co-localization between BRD4 and the GBP gene cluster by IF and DNA-FISH, and merged channels (overlapping signal in white) are shown in separate images. The dashed line highlights the nuclear periphery, determined by DAPI staining. The rightmost column shows the area in the yellow box in greater detail. Each cell type, we counted 60 GBP gene loci, 18.3% (11/60) GBP loci were co-located with BRD4 in Thp1-macro cells and 65.0% (39/60) GBP loci were co-located with BRD4 in Thp1-M.tb cells.

**Fig. 5**

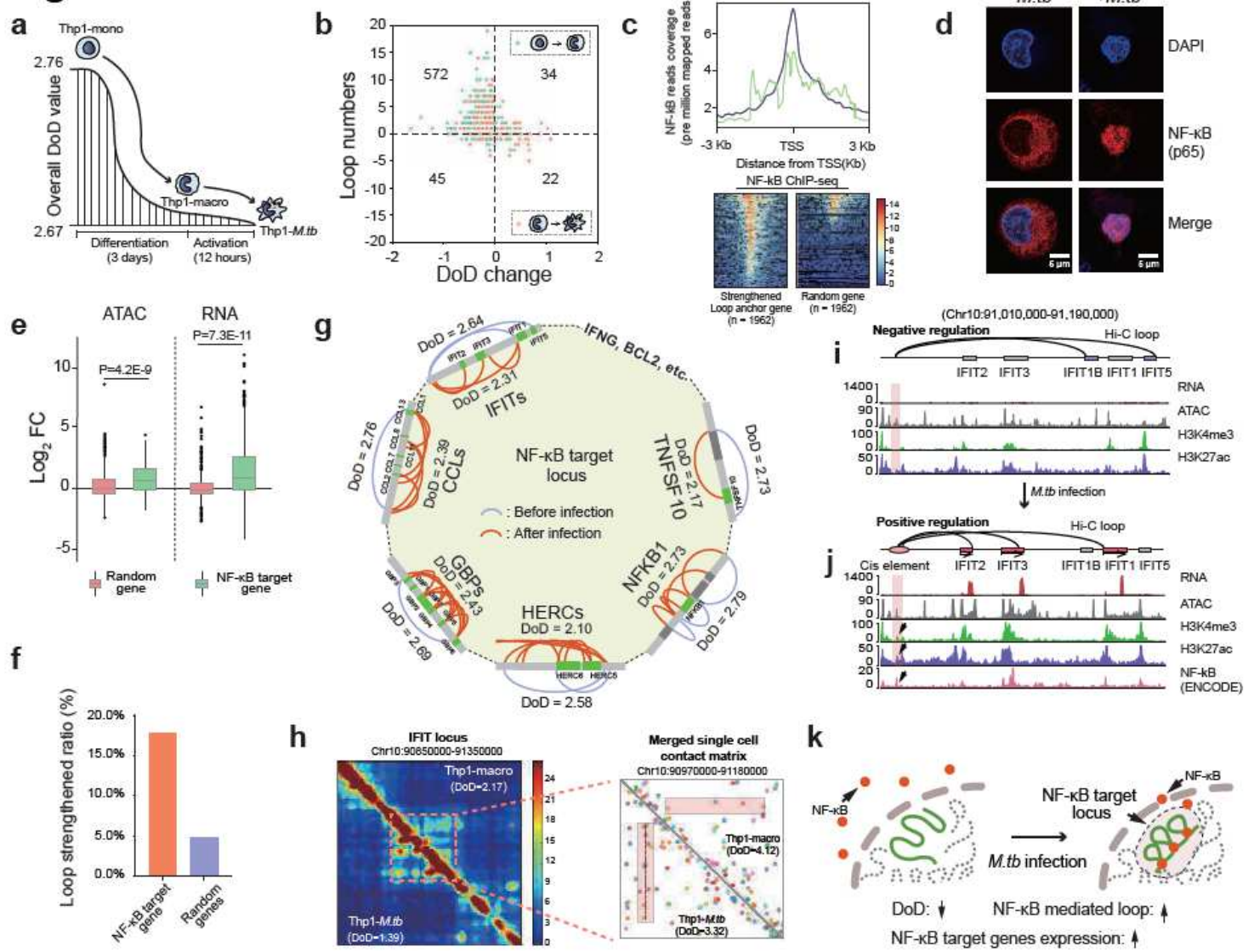


**Figure 5**

Reorganization of chromatin architecture around NF- $\kappa$ B target gene sites. a, Overall TAD DoD of THP-1 cells during differentiation and infection. The y-axis represents the average DoD value of TADs in each state. b, The relationship between TAD DoD and chromatin loop during differentiation and activation. The x-axis represents log2 fold change of TAD DoD value, and the y-axis represent the number of loop changes in each TAD. c, Compare NF- $\kappa$ B enrichment around transcription start site ( $\pm$  3 Kb) between strengthened loop anchor gene and random control gene. The gene in the heatmap were sorted according to the enrichment intensity of NF- $\kappa$ B. ChIP-seq data is from ENCODE (GM12891 cell line). d, Immunofluorescence analysis of NF- $\kappa$ B (p65) subcellular location before and after M.tb infection. e, Log2 fold changes of ATAC peaks and RNA expression level of NF- $\kappa$ B target genes ( $n=435$ ) and random control genes. Significant differences were calculated by unpaired one-sided t test. f, The ratio of strengthened loop/total loop of NF- $\kappa$ B target gene sties and random control sites. g, Chromatin loop remodeling and TAD DoD changes in typical NF- $\kappa$ B target gene loci. h, Bulk cell and merged single cell chromatin interaction matrices around IFIT gene locus. Cells with more consistent chromatin interaction were marked with a dashed line. i,j, Comparison of chromatin loop configurations, RNA expression levels, and epigenetic modifications of the IFIT gene family locus before (i) and after (j) M.tb infection. The arrows in (j) indicate the potential cis element linked with IFIT2, IFIT3, and IFIT1. k, Schematic diagram of chromatin remodeling of NF- $\kappa$ B target genes during infection.

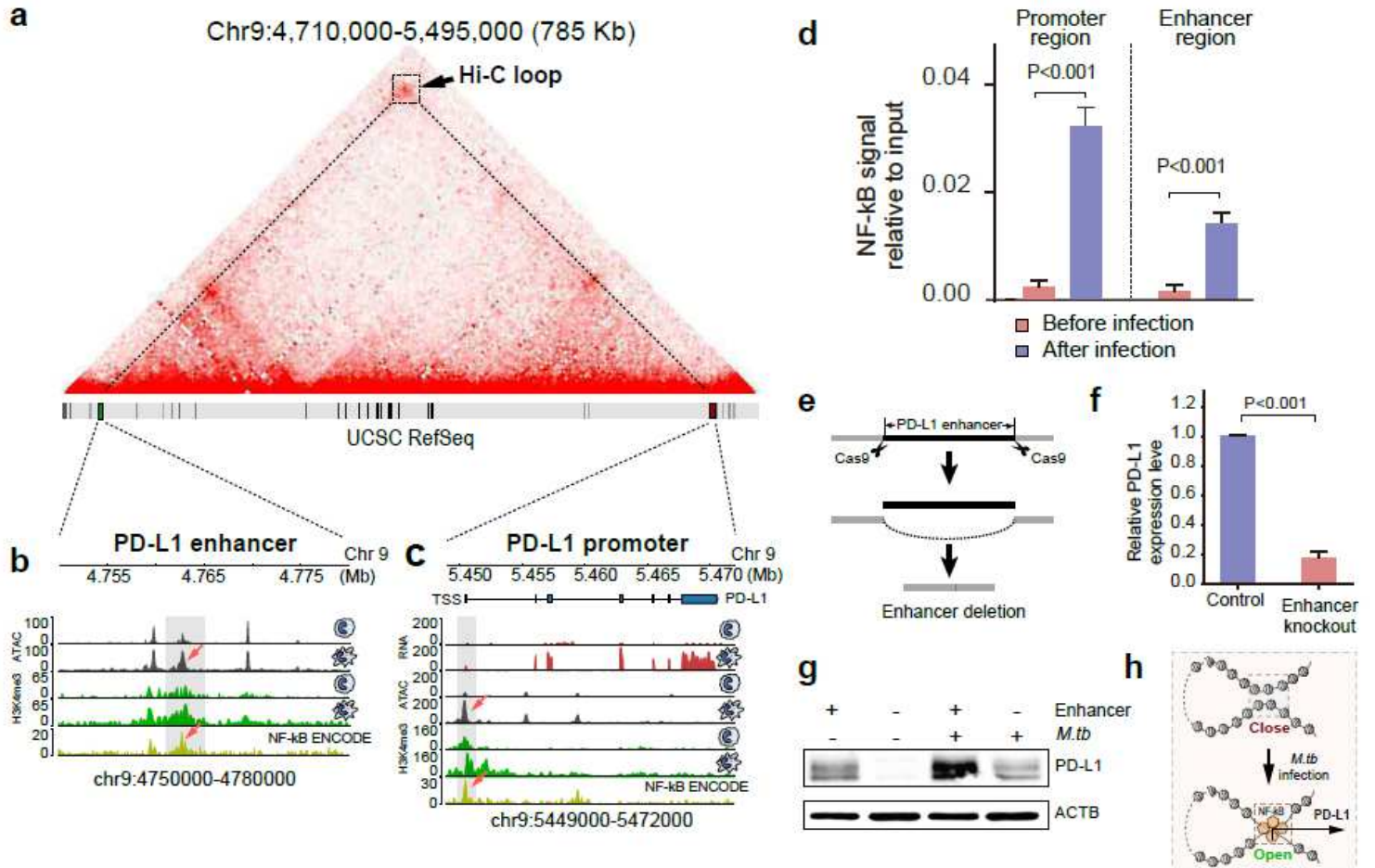


Figure 6

Functional identification of PD-L1 enhancer. a, Interaction of the PD-L1 enhancer and promoter in the Hi-C matrix. b,c, Genome Browser view of RNA expression levels, chromatin accessibility, and histone modifications at the PD-L1 gene and enhancer regions in Thp1-macro and Thp1-M.tb cells. NF- $\kappa$ B ChIP-seq peaks (ENCODE, GM15510 cell line) and strengthened ATAC-seq peaks were marked by arrows. d, ChIP-qPCR validation of the NF- $\kappa$ B (P65) enrichment on the PD-L1 enhancer and promoter regions. The amount of immunoprecipitated DNA in each sample is represented as signal relative to the total amount of input chromatin (y-axis). Significant differences were calculated by unpaired one-sided t test. e, Experimental design of sgRNA-guided enhancer perturbation by the Cas9 protein. f, Relative mRNA expression levels of PD-L1 in Thp1-macro cells and the same line after enhancer deletion. Error bars show mean  $\pm$  SE of results of three replicates; the difference was assessed using unpaired one-sided t test. g, PD-L1 protein levels in Thp1-macro cells and the same cell line after enhancer deletion before and after M.tb infection. h, Schematic of enhancer-promoter interaction mediated regulation of PD-L1 expression during M.tb infection.

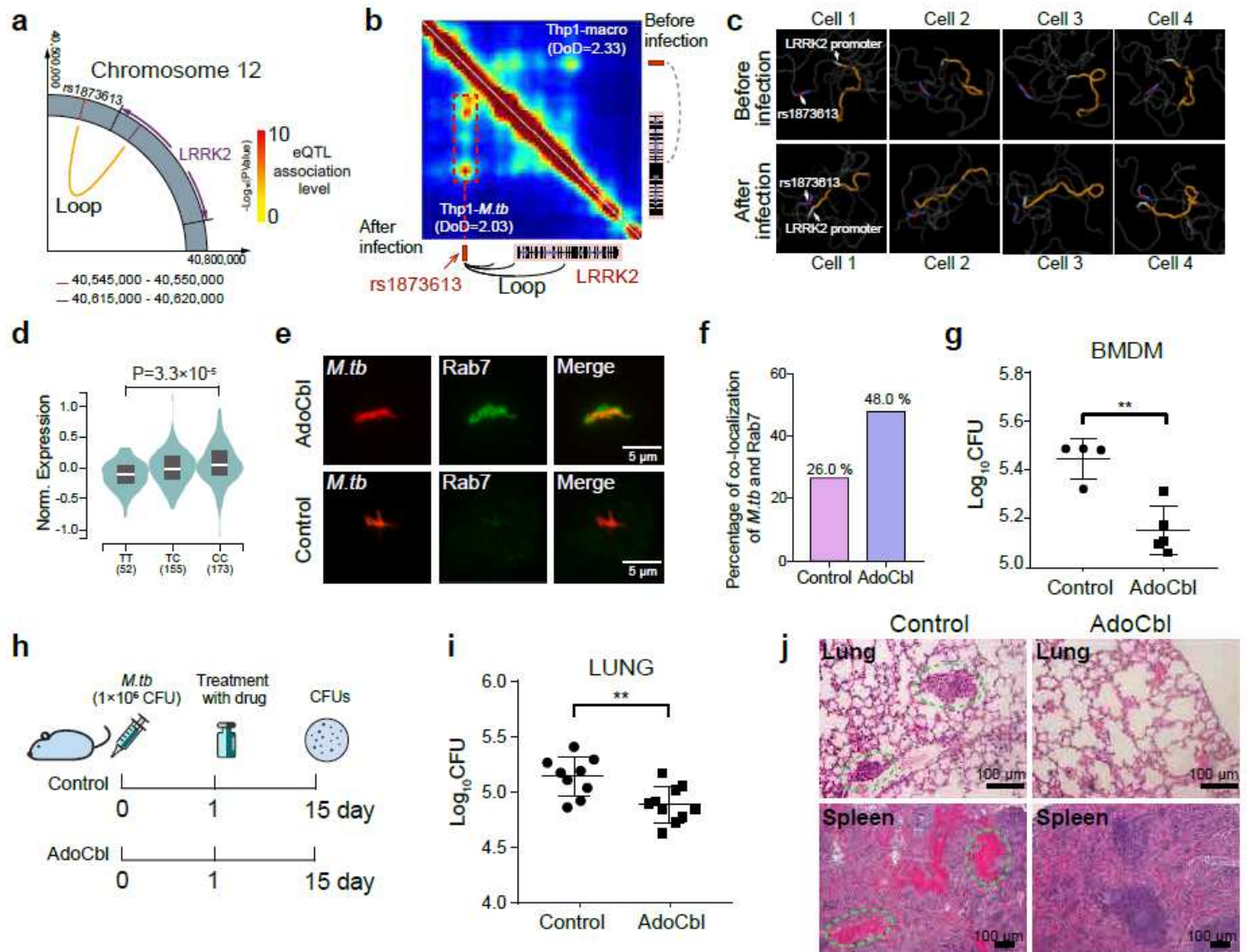


Figure 7

Identification of long range regulatory target genes of TB susceptibility loci and novel anti-TB drug targets by integrated multi-omics analysis. a, Identification of long range regulatory target genes of TB susceptibility loci, LRRK2 by integrated eQTL, Hi-C and GWAS multi-omics analysis. b, The rs1873613 SNP is located in the anchor of the LRRK2 gene chromatin loop, which is significantly strengthened after M.tb infection, as shown in the Hi-C matrix. c, Simulated typical single cell chromatin structure of SNP rs1873613 and LRRK2 gene region before and after M.tb infection. d, Regulation of LRRK2 gene expression by the rs1873613 SNP. The x axis indicates three genotypes of individuals from the Genotype-Tissue Expression (GTEx) dataset. e,f, Immunofluorescence analysis and quantification of the co-localization of the M.tb (H37Ra-RFP) and Rab7 in bone marrow-derived macrophages treated with the LRRK2 inhibitor AdoCbl and PBS (control). g, CFU assays of M.tb in bone-marrow-derived macrophage cells treated with AdoCbl and PBS (control). Significant differences were calculated by unpaired one-sided t test. h,i, CFU assays of M.tb in C57BL/6 mouse lungs treated with AdoCbl and PBS (control). Significant differences were calculated by unpaired one-sided t test. j, HE-stained lung and spleen sections in the AdoCbl and control (PBS) groups. Obvious lesions in the lungs and spleen are highlighted by the dashed lines.

## Supplementary Files

This is a list of supplementary files associated with this preprint. Click to download.

- [NSMCFigS1S7.pdf](#)
- [TableS1ThpThpp.xlsx](#)
- [TableS2THPPRa.xlsx](#)
- [TableS3sciDLOHiCdata.pdf](#)
- [TableS4BulkcellHiCdata.pdf](#)
- [TableS5promoterstatechange.xlsx](#)
- [TableS6Loopanchorgene.xlsx](#)
- [TableS7SNPinformation.xlsx](#)
- [TableS8Linkeradapterandprimer.xlsx](#)